MSC-06834

NASA TECHNICAL MEMORANDUM

NASA TM X-58091
April 1972

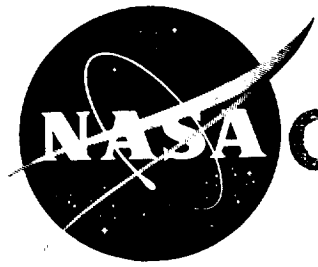

RADIATIVE HEATING TO THE APOLLO COMMAND MODULE: ENGINEERING PREDICTION AND FLIGHT MEASUREMENT

NATIONAL AERONAUTICS AND SPACE ADMINISTRATION

MANNED SPACECRAFT CENTER

HOUSTON, TEXAS 77058

NASA TM X-58091

RADIATIVE HEATING TO THE APOLLO COMMAND MODULE: ENGINEERING PREDICTION AND FLIGHT MEASUREMENT

R. C. Ried, Jr., W. C. Rochelle, and J. D. Milhoan
Manned Spacecraft Center
Houston, Texas 77058

ABSTRACT

During atmospheric entry, the Apollo command module experiences both convective heating and thermal radiation from shock-heated air. In this paper, the theory and engineering techniques that have been used for the prediction of the Apollo entry thermal-radiation environment are presented. The radiation predictions are shown to be in satisfactory agreement with the Apollo 4, FIRE I, and FIRE II flight radiometer data. The characteristics and performance of the Apollo flight radiometer and ablator-mounted configuration were determined through arc-jet simulation tests.

CONTENTS

TABLE

FIGURES

RADIATIVE HEATING TO THE APOLLO COMMAND MODULE: ENGINEERING PREDICTION AND FLIGHT MEASUREMENT

By R. C. Ried, Jr., W. C. Rochelle,* and J. D. Milhoan
Manned Spacecraft Center

SUMMARY

The theory and engineering techniques that have been used to predict radiative heating rates to the Apollo command module during entry are discussed in this paper. Discussions are given on the Apollo flow-field regimes, the radiative emission characteristics of air, the entry radiative heating predictions to the Apollo command module (including the distribution over the command module at various angles of attack), and the radiometer flight measurements. The characteristics and performance of the Apollo flight radiometer and ablator-mounted configuration were determined through simulation tests at the NASA Manned Spacecraft Center 1.5-megawatt arc-jet facility. The radiation predictions incorporate the NASA Ames Research Center four-band equilibrium radiation model, use a nonequilibrium radiation model with collision limiting, and include the effects of three-dimensional shock curvature and nonadiabatic flow. The radiation predictions are shown to be in satisfactory agreement with the Apollo 4, FIRE I, and FIRE II radiometer data. A computer program for automating the radiative heating predictions is described.

INTRODUCTION

During atmospheric entry, the Apollo command module (CM) experiences both convective heating and thermal radiation from the shock-heated air. At orbital entry speeds, this radiative heating is negligible, and at lunar-return conditions, it is only of secondary importance. However, if the Apollo CM were to enter the earth atmosphere at speeds characteristic of a return from planetary missions, thermal radiation would dominate the entry heating. Radiation from the shock-layer air is extremely sensitive to flight conditions.

Predictions of radiative heating varied significantly during the period of preliminary design to operational status of the Apollo spacecraft. The variations reflect progress both in comprehension of basic phenomena and in the engineering techniques used to describe the entry environment. Specifically, there is an improved understanding of the nonequilibrium region behind a strong shock and its associated radiation, the basic

*Formerly with TRW, Inc.; now with Tracor, Austin, Texas 78721.

characteristics of three-dimensional flow, high-temperature-air thermodynamics and chemical kinetics, the emission and absorption characteristics of air, and the interaction between radiation and the gas flow. A detailed consideration of all these factors is beyond the scope of this report; however, their relationship with engineering calculation techniques will be presented.

The objectives of this paper are to review the approximations and engineering techniques used to obtain radiative heating rates q for the Apollo CM, to present the CM flight measurements of visible and infrared radiation, and to correlate flight-observed deviations of the nonequilibrium radiation from binary-scaling relations. The gas dynamics and flow characteristics for the Apollo CM will be considered first.

FLOW FIELD

Basically, the Apollo CM is an axisymmetric vehicle with the center of gravity offset from the body axis. This arrangement produces hypersonic trim at an angle of attack (ref. 1) and results in a complex three-dimensional flow field. Because it is currently impossible to duplicate the Apollo flight conditions experimentally in ground facilities (ref. 2), a description of the flow field about the Apollo CM at flight conditions must be obtained either analytically or by empirical extrapolation from ground-facility data.

Numerical descriptions of the inviscid, three-dimensional flow of air around blunt configurations have been developed recently (refs. 3 to 5), but these programs are extensive and quite complex. Therefore, the operational use of these programs at a variety of flight conditions and angles of attack is somewhat impractical. However, the numerical programs are quite valuable in providing a check on approximate techniques. Engineering modifications have been applied to two-dimensional flow-field programs to approximate the three-dimensional characteristics of the Apollo flow field, but these programs have been limited to restricted regions of the flow, such as the flow in the pitch plane (ref. 6). In addition, geometrical constructions of the shock shape have been made as a result of observations in the NASA Ames Research Center (ARC) free-flight ballistic facility (refs. 7 and 8). This type of facility can simulate all important parameters except the vehicle scale.

In the present work, the flight flow field was obtained by extrapolation from data obtained in the Apollo wind-tunnel testing program (ref. 9). The pitch-plane shock shape at wind-tunnel conditions was obtained from schlieren photographs such as those of figure 1. The local shock-standoff distance X_N was measured normal to the body surface and normalized by the normal shock-standoff distance X_S. The measured values for the pitch plane for three angles of attack are shown in figure 2. The shock was assumed to have a sinusoidal variation about the vehicle axis as illustrated in figure 2 for two planes other than the pitch plane. It was also assumed that, for a given angle of attack, this dimensionless shock-standoff representation was invariant with flight conditions. This assumption enables the shock shape to approach the vehicle shape as the shock-layer thickness decreases.

Under these assumptions, the problem of obtaining a shock shape at flight conditions is reduced to a determination of the normal shock-standoff distance. Because the Apollo CM is a blunt configuration, it was assumed that the variation of the Apollo shock-layer thickness was proportional to that of a sphere. The scaled normal shock thicknesses measured in the wind tunnel at the location shown in figure 3 correspond to the predicted stagnation-point-standoff distances for the spheres of radii given in figure 4. The stagnation-point-standoff distances for a sphere at flight conditions were obtained from the application of an equilibrium air, inviscid, axisymmetric flow-field solution (ref. 10). The calculated stagnation-point shock-standoff distances are shown in figure 5 as a function of flight conditions. Also, the Apollo 4 flight trajectory is shown in figure 5 for reference. In the initial phase of this work, the sphere shock-standoff distances were obtained from an analytical flow-field solution that assumed a constant-density shock layer. This approximate solution gave the sphere-shock-standoff distance as a unique function of the normal shock-density ratio. This simple analytical prediction, shown in figure 6, provides a reasonable correlation of the flow-field calculations (also shown in figure 6).

With the shock shape and location defined, the real air conditions immediately downstream of the shock are determined uniquely. The air conditions at the vehicle surface can be obtained readily by assuming an isentropic and adiabatic expansion from stagnation conditions to the local surface pressure. The local surface pressure is obtained from the wind-tunnel data (refs. 2, 11, and 12). The boundaries of the shock layer are then defined completely, subject to the previously mentioned assumptions.

FLOW REGIMES

The significant aerodynamic forces and heating to the Apollo CM occur in the continuum flow regime (ref. 13). However, at high-altitude flight conditions, the chemical and thermodynamic reaction times are comparable to the characteristic flow times. In addition, at the more severe flight conditions, there is a coupling between the gas dynamic flow and the energy transport by thermal radiation. Both of these interactions have a second-order effect on the gas dynamic flow fields; however, they have a significant effect on the radiative heating.

In reality, the air immediately behind a strong shock is not in chemical or thermodynamic equilibrium (ref. 13). The extent of this nonequilibrium region has been determined by measurement of the associated radiation for one-dimensional flow behind normal shocks (ref. 14). The characteristic distance for the radiation to relax to 110 percent of the corresponding equilibrium intensity $\delta_{0.1}$ is shown as a function of altitude and velocity in figure 7. Although the data from reference 10 (indicated in fig. 7) were obtained at shock-tube conditions, it is assumed that the measured distances are applicable to the decelerating flow in front of an entry vehicle. Also, it is assumed that the presence of the nonequilibrium region behind the shock does not affect the value of the shock-standoff distance calculated for complete equilibrium conditions. However, the thickness of the air radiating at equilibrium conditions is then reduced from the shock-standoff distance by the nonequilibrium relaxation distance. If the relaxation distance is greater than the calculated shock-standoff distance, the equilibrium radiation does not exist. The resulting equilibrium air thickness is shown in figure 8 for a

10-foot-radius sphere that corresponds approximately to the CM at a 24.4° angle of attack. The values shown in figure 8 have been used only at the normal shock location; away from the normal shock location, the nonequilibrium distances of figure 7 were applied along a streamline, based on the local oblique-shock normal-component velocity.

As can be seen for the Apollo 4 trajectory shown in figure 7, the nonequilibrium region is only a fraction of the shock-layer thickness during the period of the major deceleration and heating. This nonequilibrium region (relaxation distance) is compared with the equilibrium and total shock-standoff distances for the Apollo 4 flight in figure 9. Thus, the Apollo CM, with a ballistic number of 78 lb/ft^2, flies on the border of low-density-flow effects. Collision limiting of the thermal radiation has been considered only empirically and only for the nonequilibrium radiation as discussed in the next section. The Apollo flight conditions and the blunt Apollo configuration also allow the neglect of viscous flow or boundary layer effects (refs. 13 and 15).

The state of the air in the shock layer is established uniquely by the mass, momentum, and energy flux associated with a particular flight condition. The thermal radiation emitted by high-temperature air can reach local energy-flux levels that are comparable to the total local gas energy flux. This coupling has been termed nonadiabatic flow and has been discussed by a number of authors (e.g., refs. 16 to 20). Although the state of the art in inviscid gas-dynamic flows has reached the point of considering three-dimensional flow (refs. 3 and 4), the state of the art in radiation transfer is still at the one-dimensional level (refs. 21 to 23). Actually, if the local thermal radiation is not at the black body or Planck level, the radiation is not in thermodynamic equilibrium. It is fortunate that this case can be considered in a one-dimensional problem.

In this work, the nonadiabatic effects have been approximated by nonadiabatic factors ($q/q_{adiabatic}$). These factors were obtained by the use of a numerical program developed by Chin (refs. 6 and 17). The program has a two-band spectral absorption coefficient model that enables the simultaneous treatment of optically thin and optically thick radiation. Calculations were performed for selected flight conditions that enabled the construction of the nonadiabatic factors shown in figure 10. The nonadiabatic factors for the optically thin representation of the visible and infrared radiation are shown in figure 10(a), and the nonadiabatic factors for the optically thick ultraviolet emission are shown in figure 10(b). This spectral division will be discussed further in the following section.

Although this relatively crude treatment of the radiation/gas dynamics coupling is satisfactory for Apollo flight conditions, it is evident from the factors shown in figure 10 that this interaction can be very important at more severe entry conditions. Also, all precursor effects have been neglected for Apollo flight conditions.

EMISSION CHARACTERISTICS OF AIR

A comprehensive discussion of the thermal-emission characteristics of air is far beyond the scope of this paper. In one sense, however, these characteristics are the basis for the calculation of radiative heating. Ideally, calculations of radiative heating

should be based on a completely accurate and detailed knowledge of the emission characteristics of air at all possible conditions. However, it is impractical to combine such information with the requirements for a flexible engineering calculation of radiative heating. A good combination of these conflicting requirements has been obtained recently by Page, et al. (ref. 16) for the calculation of nonadiabatic equilibrium air radiative heating.

At the onset of the Apollo Program, the emission characteristics of equilibrium air had been well characterized (refs. 24 and 25) for temperatures as high as 8000° K. These results had been extrapolated to higher temperatures with considerable accuracy in terms of the radiative heating numbers (ref. 26). This agreement is somewhat fortuitous, however, when the uncovering of the ultraviolet deionization radiation by Nardone et al. (ref. 27) and the importance of atomic line radiation by Biberman et al. (refs. 28 and 29) are considered. The work of Allen (refs. 30 and 31) should be noted also as his analysis and graphs include both line radiation and self-absorption effects. In general, in the nearly 10 years since the initial air-radiation predictions of references 24 and 25, an increase in radiative heating predictions has occurred because of the incorporation of the nonequilibrium, atomic line, ultraviolet deionization, and precursor radiation (although this latter type of radiation is not important at Apollo entry velocities). A decrease in radiative heating has occurred through the incorporation of radiative/convective coupling (radiative cooling or nonadiabatic flow), nongray self-absorption, ablation-products absorption, and three-dimensional shock-curvature effects. Anderson (ref. 32) gives a survey of the relative increases and decreases in radiative heating predictions during the past 10 years.

At Apollo lunar-return flight conditions, the equilibrium-air radiation is composed primarily of four relatively equal components. In the visible and infrared portions of the spectrum, there is atomic line radiation and a background continuum radiation from the N, O, N^-, and O^- free-bound and free-free processes. The molecular band radiation that is in this portion of the spectrum is a relatively small contributor during the time of maximum heating. In the ultraviolet and vacuum ultraviolet portions of the spectrum, there is optically thick line radiation and optically thick emission from atomic ion deionization (ref. 33). Although all these contributors were combined, together with the nonequilibrium radiation for radiative heating rate calculations, only the visible and infrared radiation (including the nonequilibrium) was measured during the Apollo flights. The air-radiation tables of reference 16 for adiabatic radiative heating calculations have been used for the equilibrium radiation calculations performed here (appendix A).

The nonequilibrium radiation predictions used herein are purely empirical fits to ground-facility data and flight data obtained on the Project FIRE vehicles. The concept of binary scaling was used to reduce the dependence on nonequilibrium radiation to a variation with only velocity. The velocity dependence of the nonequilibrium radiation that was used is roughly a mean of ground-facility data. The velocity variation of the integrated nonequilibrium intensity toward the vehicle used in this paper is shown in figure 11 compared with the correlations given in references 14 and 34.

However, as noted in references 35 and 36, the FIRE data are indicative of a deviation of the nonequilibrium radiation from binary-scaling relations. Whether this deviation is because of collision-limiting effects or a combination of collision limiting and truncation is not clear. The nonequilibrium relaxation distances shown in figure 7,

however, would eliminate the effect of truncation. On this basis, it was decided to correlate the FIRE nonequilibrium radiation data with pressure. It was found that the data could be correlated as a linear function of pressure for a critical pressure as high as 0.24 atmosphere where the full binary-scaled value of nonequilibrium radiation was employed. This relation is plotted in figure 12 relative to the binary-scaled velocity dependence of the nonequilibrium radiation shown in figure 11. Although the ground-facility data exhibit a large scatter around this correlation, the FIRE data shown in figure 13 do not. The nonequilibrium comparison, of course, is restricted to the first data periods for each of the flights.

Collision limiting was not considered for the equilibrium emission. The chemical, thermodynamic, and radiative reactions in the nonequilibrium region are, in general, vastly different from those of the corresponding equilibrium state. Therefore, it cannot be assumed a priori that collision limiting in the nonequilibrium flow is related simply to collision limiting in a gas that is close to equilibrium. This phenomenon in the non-equilibrium region amounts to a specific combination of reaction rates that produce less of an overshoot in radiating species concentrations.

The theoretical predictions in figure 13 were calculated specifically for the FIRE flights; however, the prediction techniques were identical to the Apollo radiative heating calculations reported here. These prediction techniques include the application of non-adiabatic factors, the equilibrium air emission characteristics reported in reference 16, and the approximate flow-field approach described previously. The predictions are in reasonable agreement with the FIRE II data. The discrepancies with the FIRE I data during the second and third data periods are not understood; however, these may be related to the FIRE vehicle dynamics (ref. 39) in which an inflight disturbance caused the angle of attack to increase from almost 0° to approximately 33° near the beginning of the second data period.

Neither ablation-products radiation nor boundary-layer absorption have been considered in this work. These effects have been estimated to be of minor importance to the Apollo CM (as discussed in appendix B), and it has effectively been assumed that these contributions would cancel each other.

RADIATIVE HEATING

Having considered all the basic factors required for the calculation of radiative heating, it is now desirable to consider what information is needed. Basically, the operational radiative heating rates together with the more significant convective heating rates (ref. 12) and the analysis of the thermal protection system (refs. 40 and 41) are used to evaluate the operational flight capabilities of the Apollo CM. Because the Apollo CM has a tailored thermal protection system, this entails, in principle, an evaluation over the entire vehicle.

Therefore, radiative heating rates are required as a function of free-stream density, vehicle velocity, vehicle angle of attack, and the location on the surface of the vehicle. In addition, the heating-rate predictions must be in a form that is flexible enough to allow rapid computation of heating through the variations of a guided Apollo entry trajectory. The approach taken was to generate a complete set of reference

radiative heating rates as a function of free-stream density and flight velocity, and then to consider all other variables as deviations from these reference values. It was decided that the stagnation point radiative heating to a 10-foot-radius sphere would be a convenient reference rate because (from fig. 4) this radius sphere corresponds to the normal shock conditions obtained on the Apollo spacecraft at a 24.4° angle of attack. This is a reasonable value for a nominal Apollo angle of attack and, fortuitously, is very close to the Apollo 4 flight angle of attack where the flight-radiometer measurement was obtained (ref. 15).

The calculations were performed with the plane-slab approximation or the one-dimensional radiation-transfer relations. The three-dimensional character of the radiation cannot be evaluated rigorously at the present time (ref. 21); however, it was approximated by optically thin three-dimensional corrections. The optically thin three-dimensional effects are shown for the equilibrium and nonequilibrium emissions in figures 14 and 15, respectively. Universal three-dimensional correction factors of 0.84 and 0.76 were used for the equilibrium and nonequilibrium radiation, respectively, because these values did not vary more than a few percent from the actual values obtained from figures 14 and 15.

The equilibrium radiation was calculated for air at equilibrium-stagnation conditions for physical thicknesses as given in figure 5. Then, these calculations were corrected by the three-dimensional factor and also by the appropriate nonadiabatic factor from figure 10. The nonequilibrium intensity shown in figures 11 and 12 was multiplied by 2π steradians to obtain the one-dimensional heat flux, then by 0.76 to account for the three-dimensional geometry, and then by the nonadiabatic factors of figure 10(b) to obtain the nonequilibrium heat flux. The equilibrium and nonequilibrium radiative heat fluxes were added together and are shown in figure 16. This is the reference radiative heating rate. This reference radiative heating rate calculation procedure has been automated as described in appendix A.

RADIATIVE HEATING DISTRIBUTION

At the present time, a rigorous calculation of nonadiabatic, three-dimensional radiative heating to an arbitrary location on the surface of the Apollo CM is beyond the state of the art. This is not a constraint on the Apollo Program because of the minor role of radiative heating; however, this remains as an important problem for future programs. A conservative engineering approximation has been used to obtain radiative heating distributions for the Apollo spacecraft. These distributions are academic from the standpoint that the only significant flight measurement was in the stagnation region of the Apollo 4 CM; however, these distributions have been used in the interpretation of other flight data (refs. 12 and 41).

Radiative heating distributions were calculated at a variety of flight conditions within the Apollo entry-flight corridor. Although the radiative heating distributions varied with flight conditions by as much as 15 percent from the reference radiative heating, this variation did not merit the complexity of a variable radiative heating distribution. The most conservative radiative heating distribution was obtained at the low-altitude (175 000 feet) low-velocity (30 000 ft/sec) limit of significant radiative heating, and this distribution was used throughout the Apollo flight corridor.

The radiative heating at a local point was obtained from three components, each by use of the plane-slab approximation. The nonequilibrium radiation was taken from figures 11 and 12. The optically thick ultraviolet radiation was taken as the Planck distribution integrated from a 0- to 0.113-micron wavelength evaluated at the local inviscid, isentropic air temperature at the surface. The optically thin emission was assumed to vary linearly across the equilibrium air thickness from the local shock conditions to the local surface conditions. These three components were calculated over the entire blunt Apollo CM surface at selected angles of attack and then ratioed to the corresponding calculation at the normal shock location of a 10-foot sphere. The resulting relative distributions are shown in figure 17. Then, this nondimensional distribution was applied to the reference radiative heating rates of figure 16 to obtain local radiative heating. These distributions are conservative by as much as 15 percent of the reference radiative heating rate when applied to the higher velocity regions of the Apollo flight corridor. This assessment is based on adiabatic calculations, whereas nonadiabatic effects would tend to flatten this distribution (ref. 17).

An estimate of the radiative heating to the conical section of the Apollo CM was indicative that this heating was three orders of magnitude less than the radiative heating to the blunt portion. Therefore, radiative heating to the conical section was neglected.

FLIGHT MEASUREMENT

Each of the unmanned command modules for the Apollo 4 and 6 missions had four radiometers located as shown in figure 18. The radiometers mounted in the heat shield consisted of a viewing port with a thermopile mounted behind a quartz window. The arrangement is illustrated schematically in figure 19. Because of the quartz window, the radiometers measured only the visible and infrared radiation, which amounts to roughly half of the significant radiation heating.

On the Apollo 6 mission, radiometer A (CA3363K) was inoperative while the data from radiometer B (CA3364K) were in the instrument noise level. The Apollo 6 CM entered the atmosphere at a degraded velocity, below that of lunar-return simulation, and, therefore, experienced negligible radiative heating.

The Apollo 4 entry trajectory is tabulated in table I. This entry was a good simulation of lunar-return conditions. Radiometer B was inoperative; the remaining radiometers were operational. Radiometers C (CA3360K) and D (CA3361K) on the conical section did not show any detectable response during entry; however, they did show a response to the dumping of excess reaction control system fuel just before splashdown. This response verified the operational status of these radiometers, and the lack of response during entry supports the engineering predictions of negligible radiation to the conical section of the CM.

Radiometer A (CA3363K) in the stagnation region on the Apollo 4 spacecraft performed well through the period of significant radiative heating but appeared to be inoperative during postflight inspection. A head-on postrecovery photograph of the radiometer is shown in figure 20. The postflight inspection of this radiometer revealed a residue in the radiometer cavity. It is not known when this residue was deposited. When the residue was removed, the radiometer was again operational. Postflight arc-jet tests performed at the NASA Manned Spacecraft Center (MSC) at approximately the same heating rate (appendix B) did not produce any residue in this cavity.

The predicted total (including the five components) radiative heating to the surface at the location of the Apollo 4 radiometer is shown in figure 21. The corresponding visible and infrared equilibrium and the nonequilibrium intensity predictions and data for this radiometer are shown in figure 22. The agreement between the predictions and the data is excellent through most of the significant radiative heating period. The small discrepancy at peak radiative heating (where the stagnation pressure was approximately 0.5 atmosphere and the stagnation temperature approximately 10 500° K) may either be caused by the inaccuracy of the nonadiabatic treatment or, more probably, by the self-absorption of the radiation by air or ablation products in the radiometer cavity. The drift in the radiometer data after the major radiative measurement is characteristic of the instrument performance as discussed in appendix B.

The deviation of the nonequilibrium radiation from binary-scaling relations, as obtained from the FIRE data, gives a good fit of this Apollo measurement. The agreement between the FIRE data and the Apollo measurement is encouraging. The overall noise level of 3 W/cm^2-sr for the entire measurement and recording system is consistent with the Apollo 6 instrument response. This noise level is reasonable considering that the Apollo 4 data are always less than 7 percent of the theoretical full-scale range of the instrument. Apart from the noise level of the instrument, it has been estimated on the basis of ground-based calibration tests that the data shown in figure 22 are within 11 percent of the actual intensity.

CONCLUDING REMARKS

In the present outline of engineering techniques used to predict the Apollo radiative heating rates, several fundamental problems have been pointed out. These include a more comprehensive knowledge of three-dimensional flows, three-dimensional radiative transfer, coupling of the radiation and gas flow, ablation effects on the flow and heating, and heating conditions away from the stagnation region or plane of symmetry. Solution of these problems requires a significant developmental effort. The emission characteristics of air are reasonably well defined for the Apollo flight regime; however, this is not necessarily the case for higher velocity entry in which the radiative heating rates may exceed the convective heating rates. Knowledge of air radiation in the Apollo flight regime has improved considerably from the time when the design heating rates for the Apollo thermal protection system had to be specified. There is a required lead time not only in the technology but also in the practical implementation of this technology.

Perhaps the greatest contribution provided by the Apollo flight-radiometer data agreement with predictions is that this provides a degree of verification of the so-called nonadiabatic effects. However, the Apollo command module experiences only second-order coupling effects, and these, unfortunately, do not provide confirmation of the first-order coupling effects predicted at higher velocities.

Manned Spacecraft Center
National Aeronautics and Space Administration
Houston, Texas, April 7, 1972
914-50-20-10-72

REFERENCES

1. Ried, Robert C., Jr.; and Mayo, Edward E.: Equations for the Newtonian Static and Dynamic Aerodynamic Coefficients for a Body of Revolution with an Offset Center-of-Gravity Location. NASA TN D-1085, June 1963.

2. Bertin, John J.: Wind-Tunnel Heating Rates for the Apollo Spacecraft. NASA TM X-1033, Jan. 1965.

3. Webb, H. G., Jr.; Dresser, H. S.; Adler, B. K.; and Waiter, S. A.: Inverse Solution of Blunt-Body Flowfields at Large Angle of Attack. AIAA, vol. 5, no. 6, June 1967, pp. 1079-1085.

4. Bohachevsky, I. O.; and Mates, R. E.: A Direct Method for Calculation of the Flow About an Axisymmetric Blunt Body at Angle of Attack. AIAA, vol. 4, no. 5, May 1966, pp. 776-782.

5. Moretti, G.; and Bleich, G.: Three-Dimensional Flow Around Blunt Bodies. AIAA, vol. 5, no. 9, Sept. 1967, pp. 1557-1562.

6. Hearne, L. F.; Chin, J. H.; and Woodruff, L. W.: Study of Aerothermodynamic Phenomena Associated with Reentry of Manned Spacecraft. NASA CR-65368, May 1966.

7. Kaattari, G. E.: Shock Envelopes of Blunt Bodies at Large Angles of Attack. NASA TN D-1980, Dec. 1963.

8. Kaattari, G. E.: Predicted Gas Properties in the Shock Layer Ahead of Capsule-Type Vehicles at Angles of Attack. NASA TN D-1423, Oct. 1962.

9. Moseley, W. C., Jr.; and Martino, J. C.: Apollo Wind Tunnel Testing Program — Historical Development of General Configurations. NASA TN D-3748, 1966.

10. Inouye, M.; Rakich, J. V.; and Lomax, H.: A Description of Numerical Methods and Computer Programs for Two-Dimensional and Axisymmetric Supersonic Flow Over Blunt-Nosed and Flared Bodies. NASA TN D-2970, Aug. 1965.

11. Lee, Dorothy B.; Bertin, John J.; and Goodrich, W. D.: Heat Transfer Rate and Pressure Measurements Obtained During Apollo Orbital Entries. NASA TN D-6028, Oct. 1970.

12. Lee, Dorothy B.; and Goodrich, W. D.: The Aerothermodynamic Environment of the Apollo CM During Superorbital Entry. NASA TN D-6792, Apr. 1972.

13. Ried, Robert C., Jr.: Aerodynamic Heating. Ch. 6 of Manned Spacecraft: Engineering Design and Operation, P. E. Purser, M. A. Faget, and N. F. Smith, eds., Fairchild Publications, Inc., 1964, pp. 45-51.

14. Anon.: Study of Thermal Radiation Associated With Non-Equilibrium Flow in the Apollo Flight Regime (U). Avco Everett Res. Lab., Doc. No. AERL 62-702, Sept. 1962.

15. Hillje, E. R.: Entry Aerodynamics at Lunar Return Conditions Obtained From the Flight of Apollo 4 (AS-501). NASA TN D-5399, May 1969.

16. Page, W. A.; Compton, D. L.; Borucki, W. J.; Ciffone, D. L.; and Cooper, D. M.: Radiative Transport in Inviscid Nonadiabatic Stagnation-Region Shock Layers. Paper 68-784, AIAA 3rd Thermophysics Conference, June 24-26, 1968.

17. Chin, Jin H.: Effects of Non-Grey Self-Absorption and Energy Loss for Blunt Body Flows. J. Quant. Spectrosc. Rad. Trans., vol. 8, Jan. 1968, pp. 503-511.

18. Wilson, K. H.; and Hoshizaki, H.: Inviscid, Nonadiabatic Flow About Blunt Bodies. AIAA, vol. 3, no. 1, Jan. 1965, pp. 67-74.

19. Dirling, R. B., Jr.; Rigdon, W. S.; and Thomas, M.: Stagnation-Point Heating Including Spectral Radiative Transfer. Proceedings of the 1967 Heat Transfer and Fluid Mechanics Institute, Stanford Univ. Press, 1967, pp. 141-162.

20. Goulard, R.: The Coupling of Radiation and Convection in Detached Shock Layers. J. Quant. Spectrosc. Rad. Trans., vol. 1, Dec. 1961, pp. 249-257.

21. Ried, R. C., Jr.: Equations of Change for a Photon Gas and Their Correspondence with Maxwell's Equations. Ph. D. Thesis, Rice Univ., 1967.

22. Cheng, P.: Study of the Flow of a Radiating Gas by a Differential Approximation. Ph. D. Thesis, Stanford Univ., 1965.

23. Cheng, P.: Two-Dimensional Radiating Gas Flow by a Moment Method. AIAA, vol. 2, no. 9, 1964, pp. 1662-1664.

24. Keck, J. C.; Camm, J. C.; Kivel, B.; and Wentink, T., Jr.: Radiation From Hot Air. Part II. Shock Tube Study of Absolute Intensities. Ann. Phys., vol. 7, no. 1, May 1959, pp. 1-38.

25. Kivel, B.; and Bailey, K.: Tables of Radiation from High Temperature Air. Res. Rep. 21, Avco Everett Res. Lab., Dec. 1957.

26. Page, W. A.; and Arnold, J. O.: Shock-Layer Radiation of Blunt Bodies at Reentry Velocities. NASA TR R-193, Apr. 1964.

27. Nardone, M. C.; Breene, R. G.; Zeldin, S. S.; and Riethof, T. R.: Radiance of Species in High Temperature Air. Rep. R 63 SD3, General Electric Co., Space Sciences Lab., June 1963.

28. Biberman, L. M.; Vorob'yev, V. S.; and Norman, G. E.: Energy Emitted in Spectral Lines by a Plasma at Equilibrium. Optika i Spektrosk. (SSSR), vol. 14, no. 3, Mar. 1963, pp. 330-335. (Eng. trans. in Optics and Spectroscopy. (USA), vol. 14, no. 3, Mar. 1963, pp. 176-179.)

29. Biberman, L. M.; Vorob'yev, V. S.; Norman, G. E.; and Yakubov, I. T.: Radiative Heating in Hypersonic Flow. Cosmic Res., vol. 2, no. 3, July 1964, pp. 130-156.

30. Allen, R. A.: Air Radiation Tables: Spectral Distribution Functions for Molecular Band Systems. Res. Rep. 236, Avco Everett Res. Lab., Apr. 1966.

31. Allen, R. A.: Air Radiation Graphs: Spectrally Integrated Fluxes Including Line Contributions and Self Absorption. Res. Rep. 230, Avco Everett Res. Lab., Sept. 1965.

32. Anderson, J. D., Jr.: An Engineering Survey of Radiating Shock Layers. Paper 68-1151, AIAA Entry Vehicle Systems and Technology Meeting, Dec. 3-5, 1968.

33. Hahne, G. E.: The Vacuum Ultraviolet Radiation from N^+- and O^+-Electron Recombination in High-Temperature Air. NASA TN D-2794, 1965.

34. Canning, T. N.; and Page, W. A.: Measurements of Radiation from the Flow Fields of Bodies Flying at Speeds up to 13.4 Kilometers per Second. Presented to Fluid Mechanics Panel of AGARD (Brussels, Belgium), Apr. 3-6, 1962.

35. Cauchon, D. L.: Radiative Heating Results from the FIRE II Flight Experiment at a Reentry Velocity of 11.4 Kilometers per Second. NASA TM X-1402, July 1967.

36. Dingeldein, R. C.: Flight Measurements of Reentry Heating at Hyperbolic Velocity (Project FIRE) (U). NASA TM X-1053, Jan. 1965.

37. Allen, R. A.; Rose, P. H.; and Camm, J. C.: Non-equilibrium and Equilibrium Radiation at Super-Satellite Re-entry Velocities. Paper 63-77, IAS 31st Annual Meeting, Jan. 21-23, 1963.

38. Teare, J. D.; Georgiev, A.; and Allen, R. A.: Radiation From the Non-Equilibrium Shock Front. Res. Rep. 112, Avco Everett Res. Lab., Oct. 1961.

39. Woodbury, G. E.: Angle-of-Attack Analysis for Project FIRE I Payload Reentry Flight. NASA TN D-3366, 1966.

40. Curry, Donald M.: An Analysis of a Charring Ablation Thermal Protection System. NASA TN D-3150, Dec. 1965.

41. Curry, Donald M.; and Stephens, Emily W.: Apollo Ablator Thermal Performance at Superorbital Entry Velocities. NASA TN D-5969, Sept. 1970.

TABLE I. - APOLLO 4 TRAJECTORY (45-DAY BEST ESTIMATED TRAJECTORY 12/20/67)

[Recommended atmosphere 1966 15° N annual
Free-stream density calculated from pressure measurements: $\rho_\infty \simeq P_{st} \Big/ \left| V_\infty^2 \left(1 - \rho_\infty / 2\rho_{st}\right) \right|$]

Time, sec	Altitude, ft	Relative velocity, ft/sec	Measured stagnation pressure, psia	Calculated free-stream density, lb/ft^3	Nonadiabatic factor at S/R = 0.732	Calculated cold-wall convective heating at S/R = 0.732, Btu/ft^2-sec
29 968	405 116	35 216			1.0	1.2
28 970	396 437	35 224			1.0	2.7
29 984	339 146	35 273			1.0	7.1
30 000	281 189	35 302	0.13	4.84×10^{-7}	1.0	32
30 004	267 999	35 292	.20	9.90	.99	46
30 010	249 265	35 236	.61	2.24×10^{-6}	.91	74
30 016	231 962	35 088	1.15	4.60	.84	107
30 020	221 358	34 909	1.85	7.08	.80	129
30 022	216 418	34 697	2.37	8.80	.785	140
30 024	211 779	34 485	3.00	1.08×10^{-5}	.770	151
30 026	207 440	34 273	3.41	1.30	.758	162
30 028	203 395	34 061	4.04	1.56	.755	179
30 030	199 638	33 848	4.60	1.87	.755	191
30 032	196 169	33 636	5.12	2.13	.756	200
30 034	193 029	33 304	5.76	2.46	.758	209
30 036	190 275	32 946	6.14	2.69	.760	212
30 038	187 921	32 560	6.70	2.91	.765	213
30 040	185 985	32 146	6.96	3.13	.771	214
30 044	183 379	31 280	7.25	3.44	.824	206
30 048	182 427	30 411	7.08	3.57	.877	191
30 052	183 008	29 583	6.68	3.50	.907	175
30 060	187 844	28 150	5.18	3.03	.972	140
30 070	194 746	26 877	3.47	2.23	1.0	103
30 080	198 675	25 933	2.77	1.93	1.0	86
30 090	199 953	25 132	2.48	1.86	1.0	76
30 100	201 129	24 413	2.17	1.70	1.0	67
30 110	205 334	23 808	1.78	1.46	1.0	57
30 120	210 270	23 329	1.38	1.20	1.0	48
30 130	215 505	22 995	1.03	9.50×10^{-6}	1.0	41
30 140	220 407	22 661	.82	7.95	1.0	36
30 150	224 824	22 430	.68	6.45	1.0	30
30 200	238 768	21 712	.37	3.74	1.0	19
30 250	241 159	21 225	.31	3.40	1.0	18
30 300	232 388	20 721	.40	4.64	1.0	20
30 320	225 166	20 454	.56	5.76	1.0	22
30 340	215 160	20 084	.79	8.97	1.0	26
30 360	202 218	19 507	1.28	1.50×10^{-5}	1.0	31
30 380	187 427	18 545	2.12	2.83	1.0	36
30 400	172 291	17 038	3.08	4.89	1.0	37
30 420	158 752	14 936	3.98	8.27	1.0	31
30 440	149 388	12 459	4.07	1.23×10^{-4}	1.0	22
30 460	142 474	10 159	3.57	1.61	1.0	13
30 480	138 772	8 266	2.72	1.89	1.0	7.3
30 500	132 555	6 741	2.48	2.53	1.0	4.5
30 520	122 432	5 327	2.52	4.09	1.0	2.7

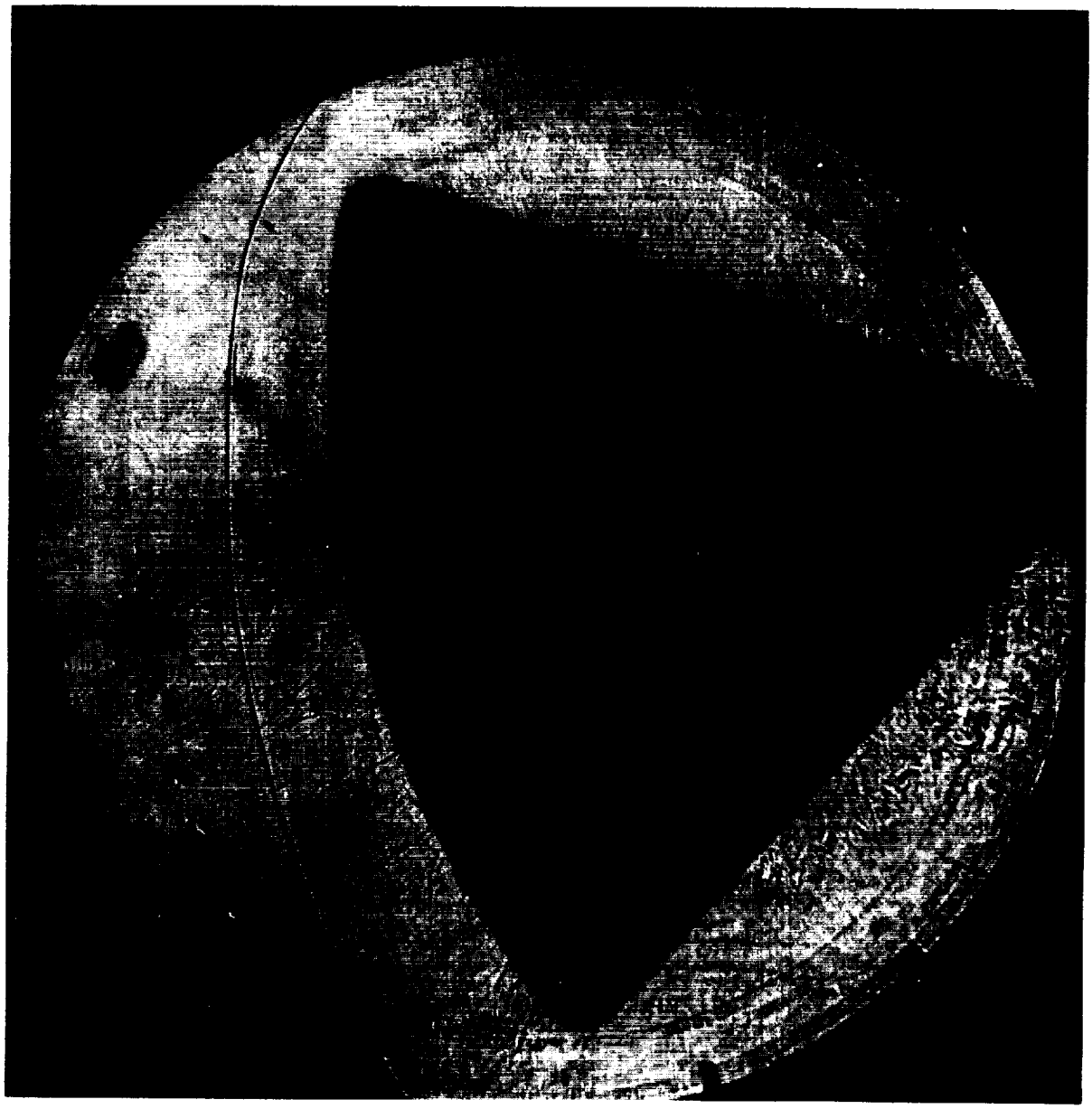

(a) $\alpha = 19°$.

Figure 1. - Schlieren photographs of the Apollo command module at various angles of attack.

(b) $\alpha = 25°$.

Figure 1. - Continued.

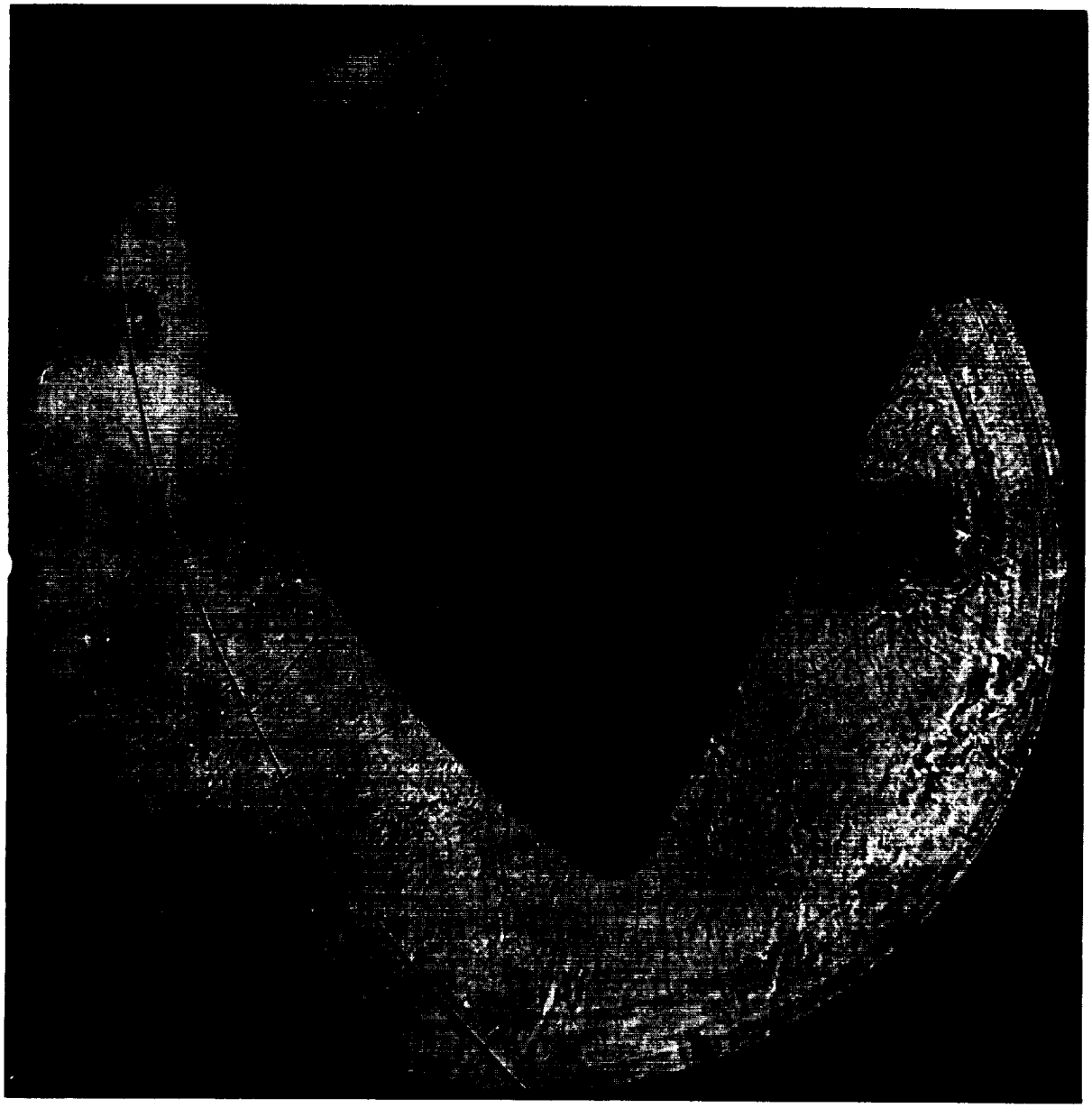

(c) $\alpha = 33°$.

Figure 1. - Concluded.

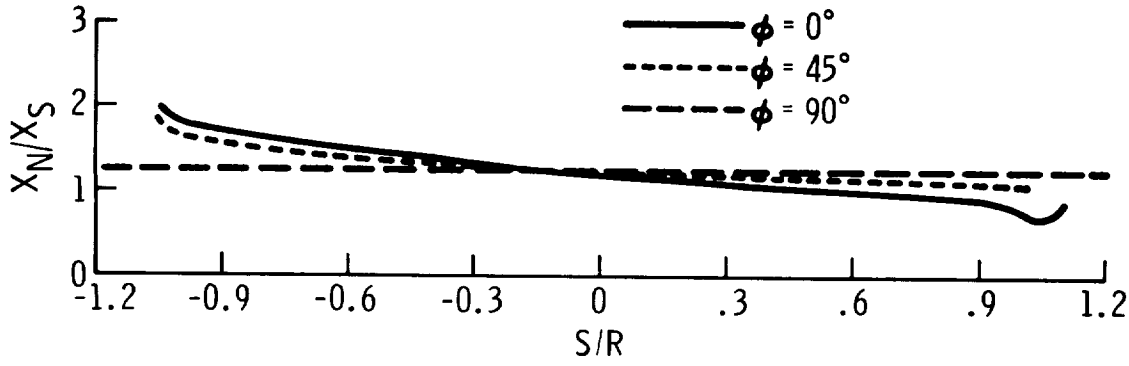

(a) α = 19°.

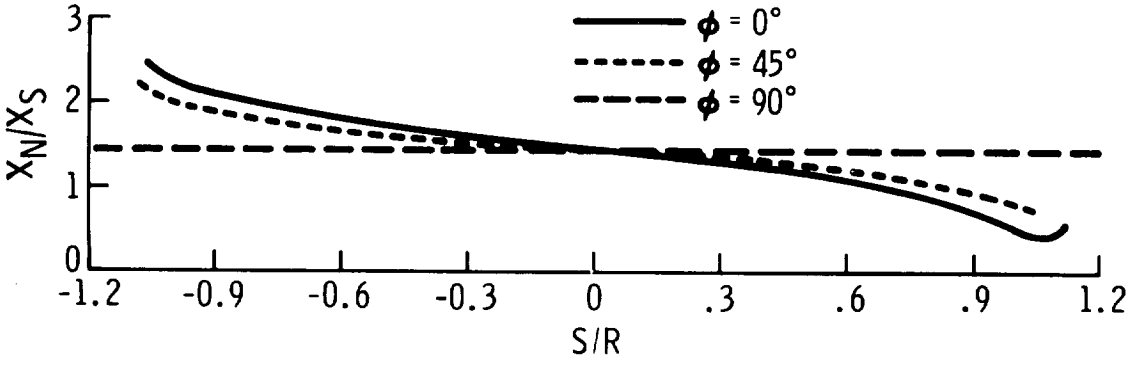

(b) α = 25°.

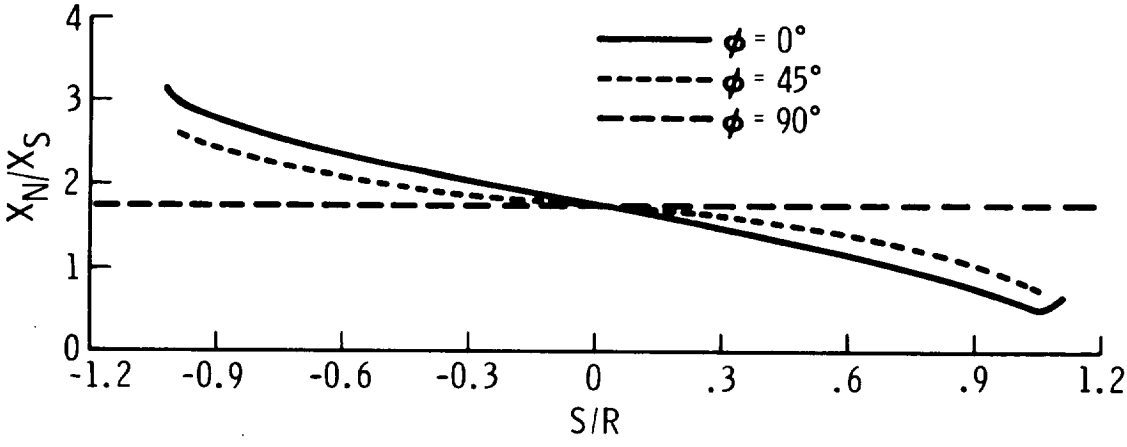

(c) α = 33°.

Figure 2.- Measured and assumed relative local shock-standoff distance for the forebody of the Apollo command module at various angles of attack (S = distance measured from center of aft compartment, ft; R = CM maximum radius measured from the X_c-axis, 6.417 ft).

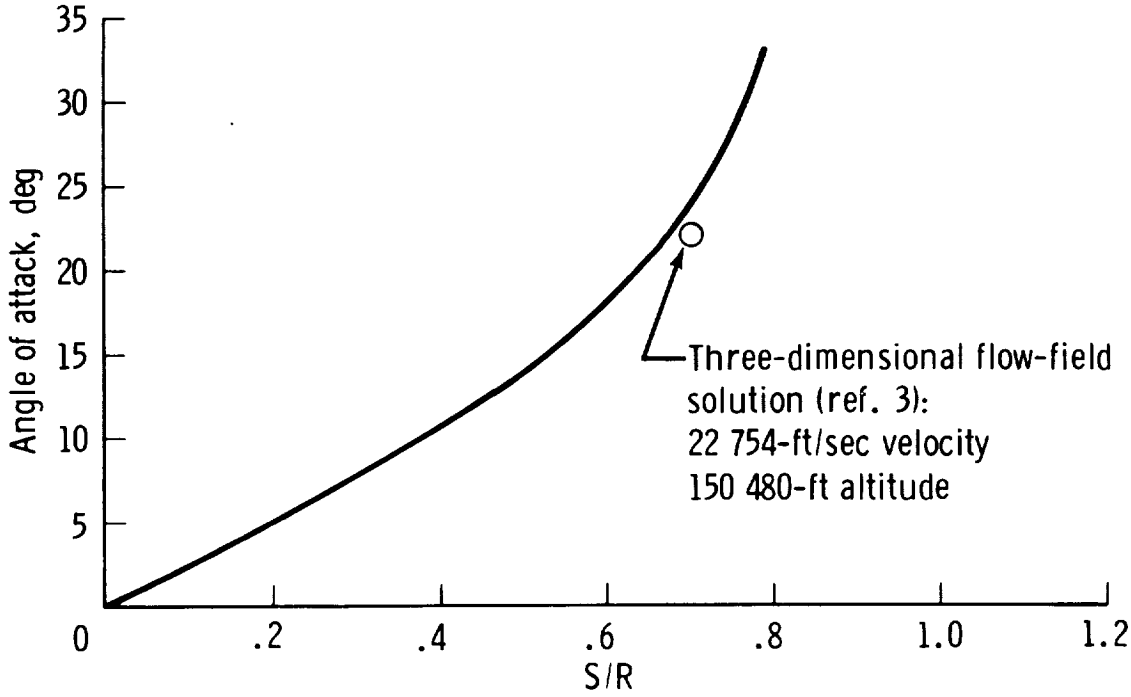

Figure 3. - Normal shock location as a function of angle of attack.

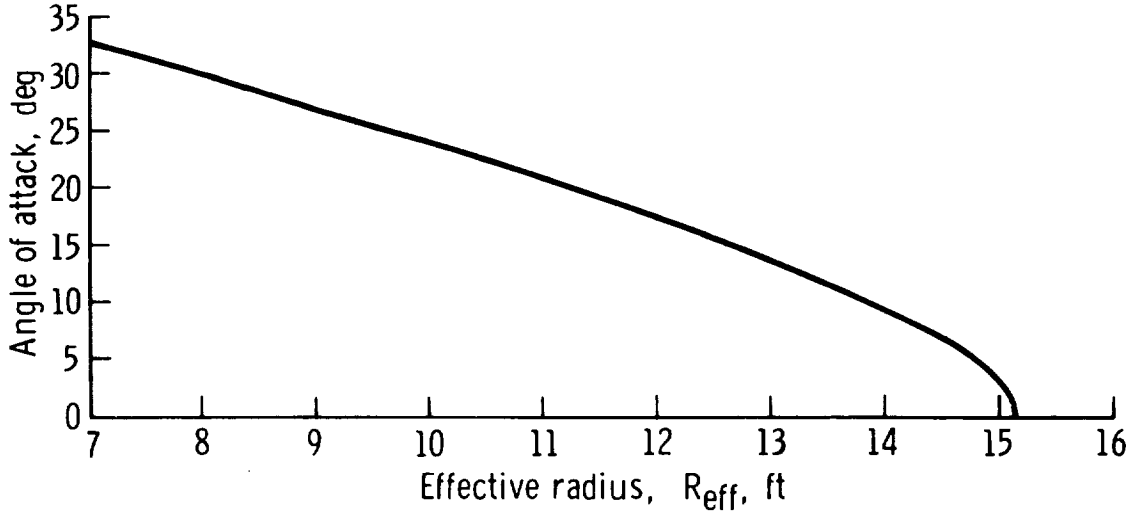

Figure 4. - Effective radius for radiative heating as a function of angle of attack.

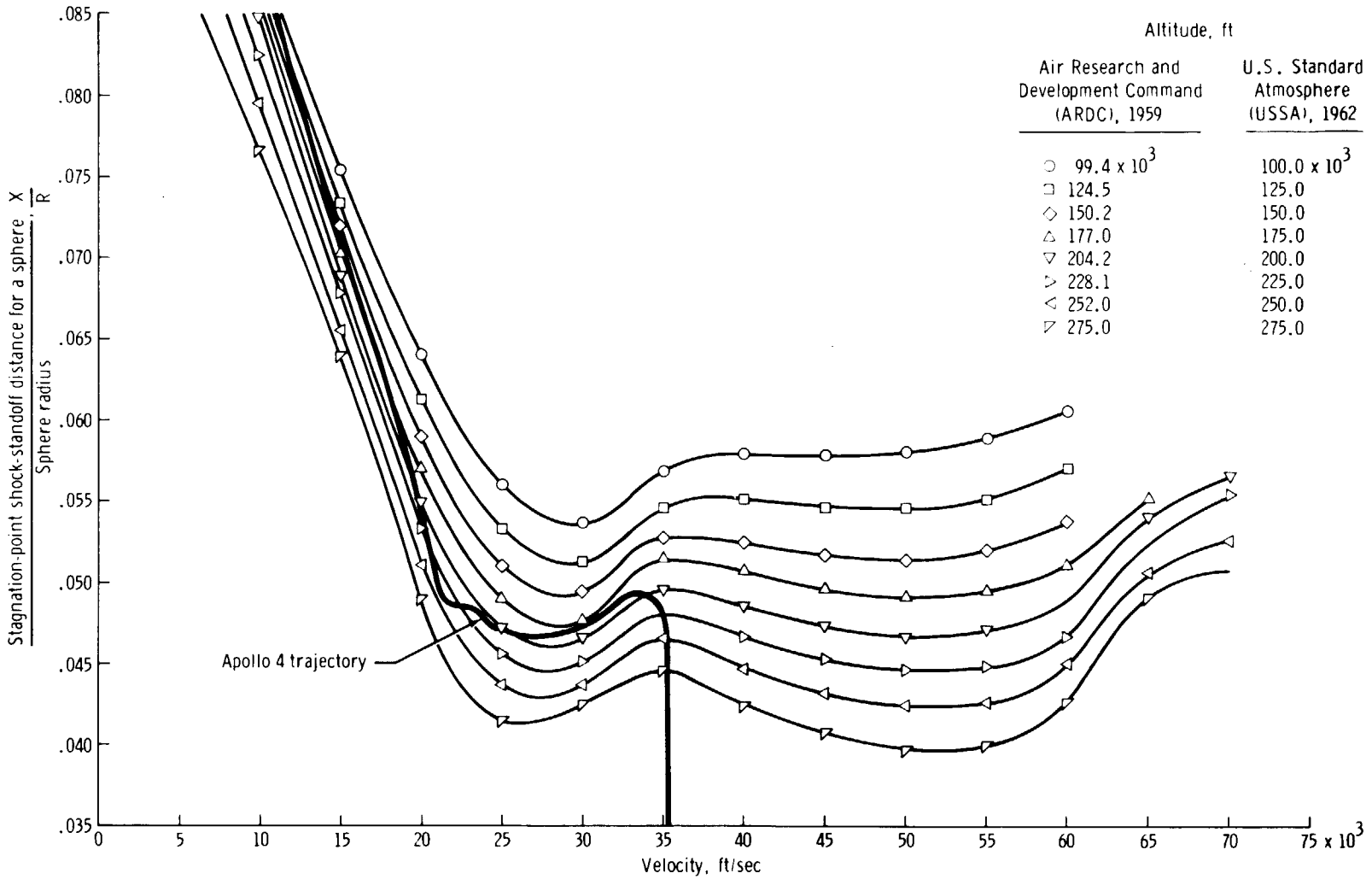

Figure 5. - Stagnation-point shock-standoff distances for a sphere as a function of velocity for various altitudes.

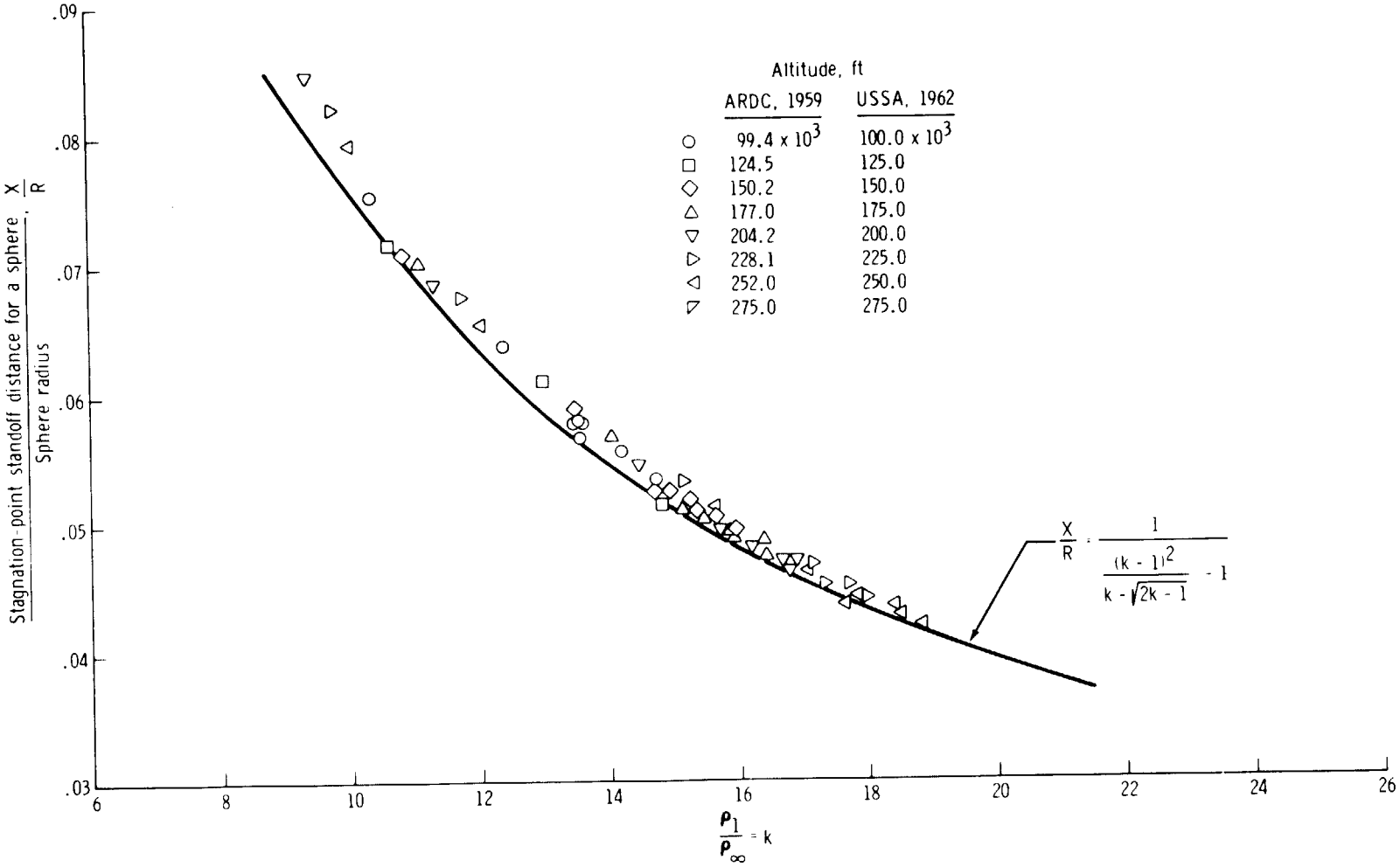

Figure 6.- Comparison of stagnation-point-standoff distances for a sphere with an empirical constant-density approximation.

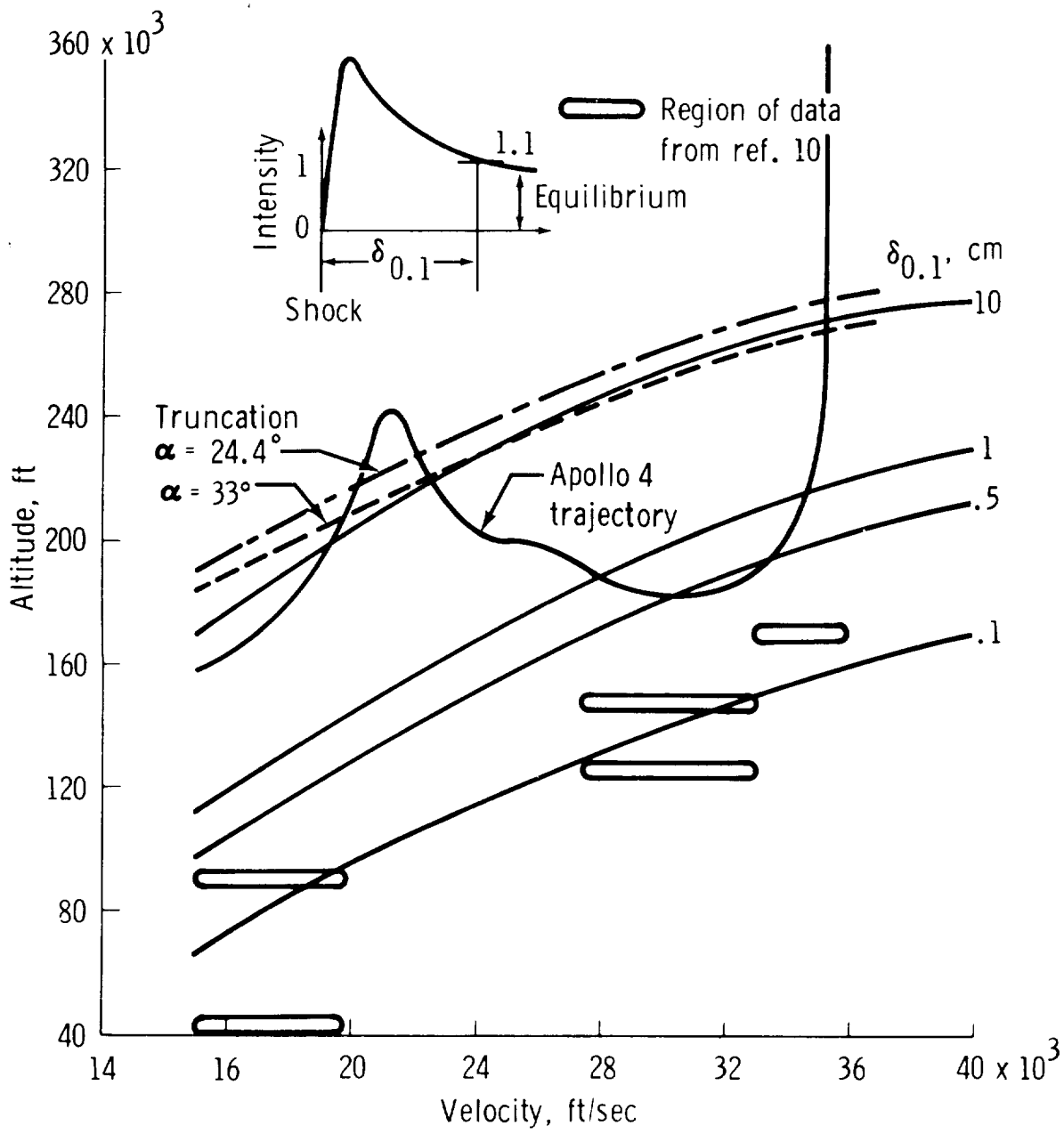

Figure 7. - Nonequilibrium relaxation distance behind a normal shock in air.

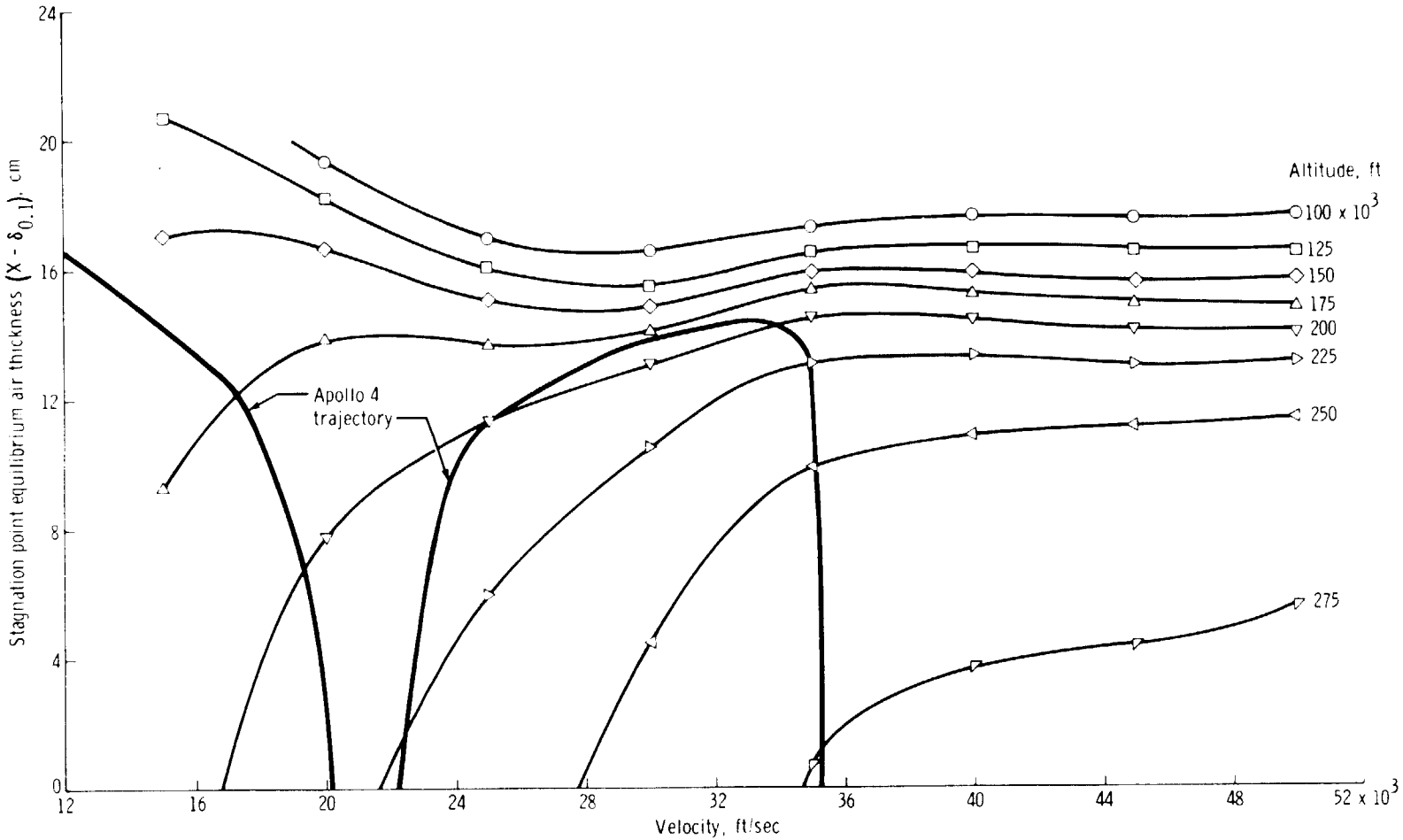

Figure 8. - Equilibrium air thickness at the stagnation point of the Apollo command module when $\alpha = 24.4^{\circ}$.

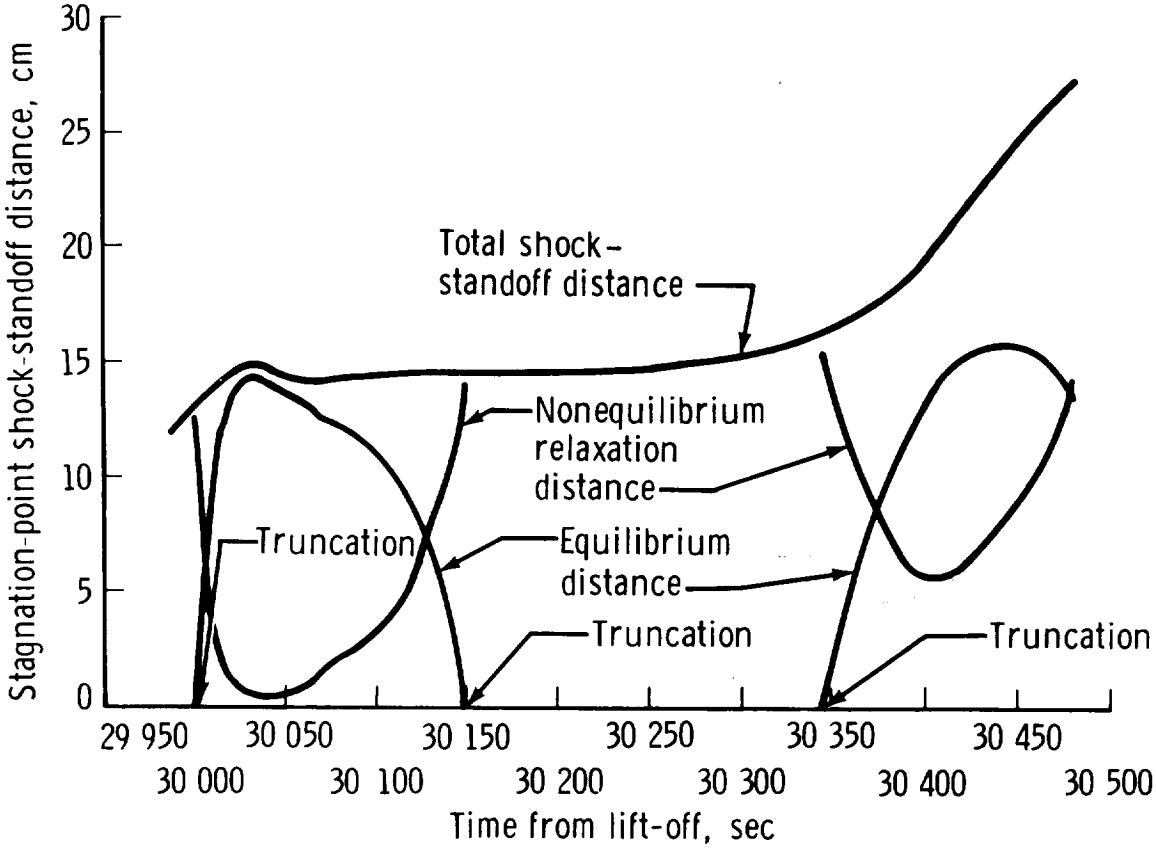

Figure 9. - Shock-standoff distance as a function of time for the Apollo 4 flight.

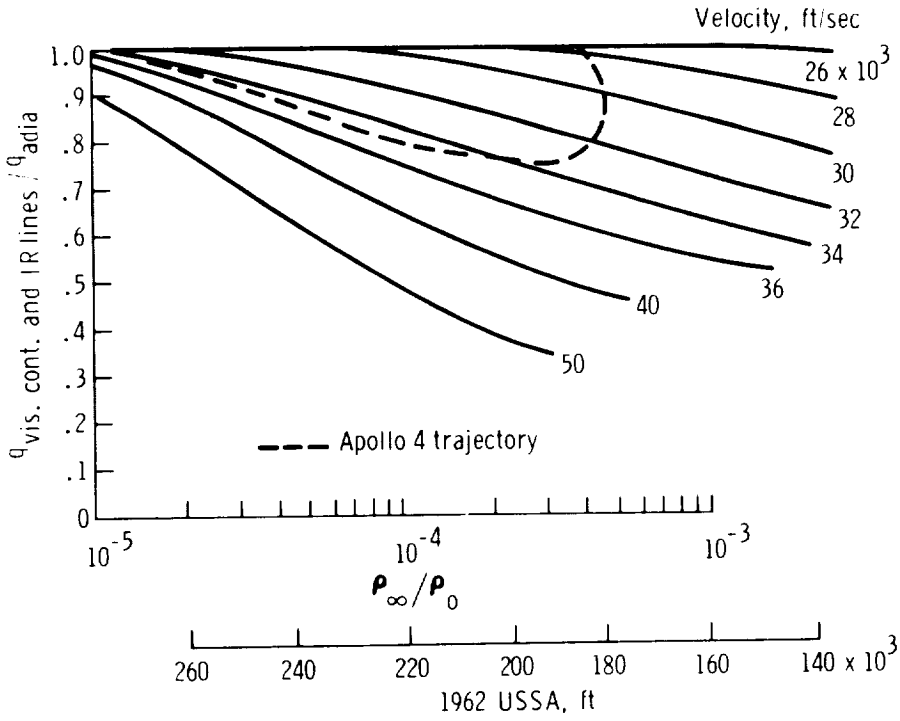

(a) For visible continuum, nonequilibrium, and infrared lines, R_{eff} = 10 ft.

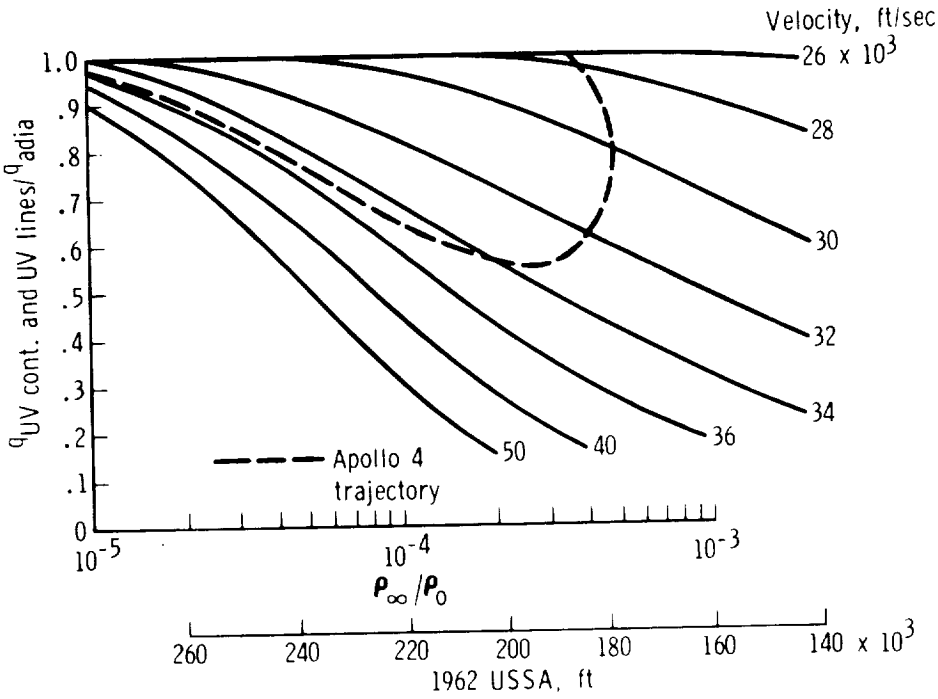

(b) For ultraviolet continuum and ultraviolet lines, R_{eff} = 10 ft.

Figure 10. - Nonadiabatic factors.

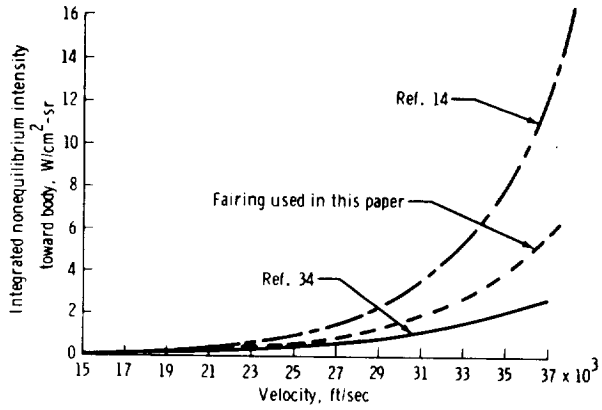

Figure 11. - Integrated nonequilibrium radiant-intensity predictions as a function of flight velocity.

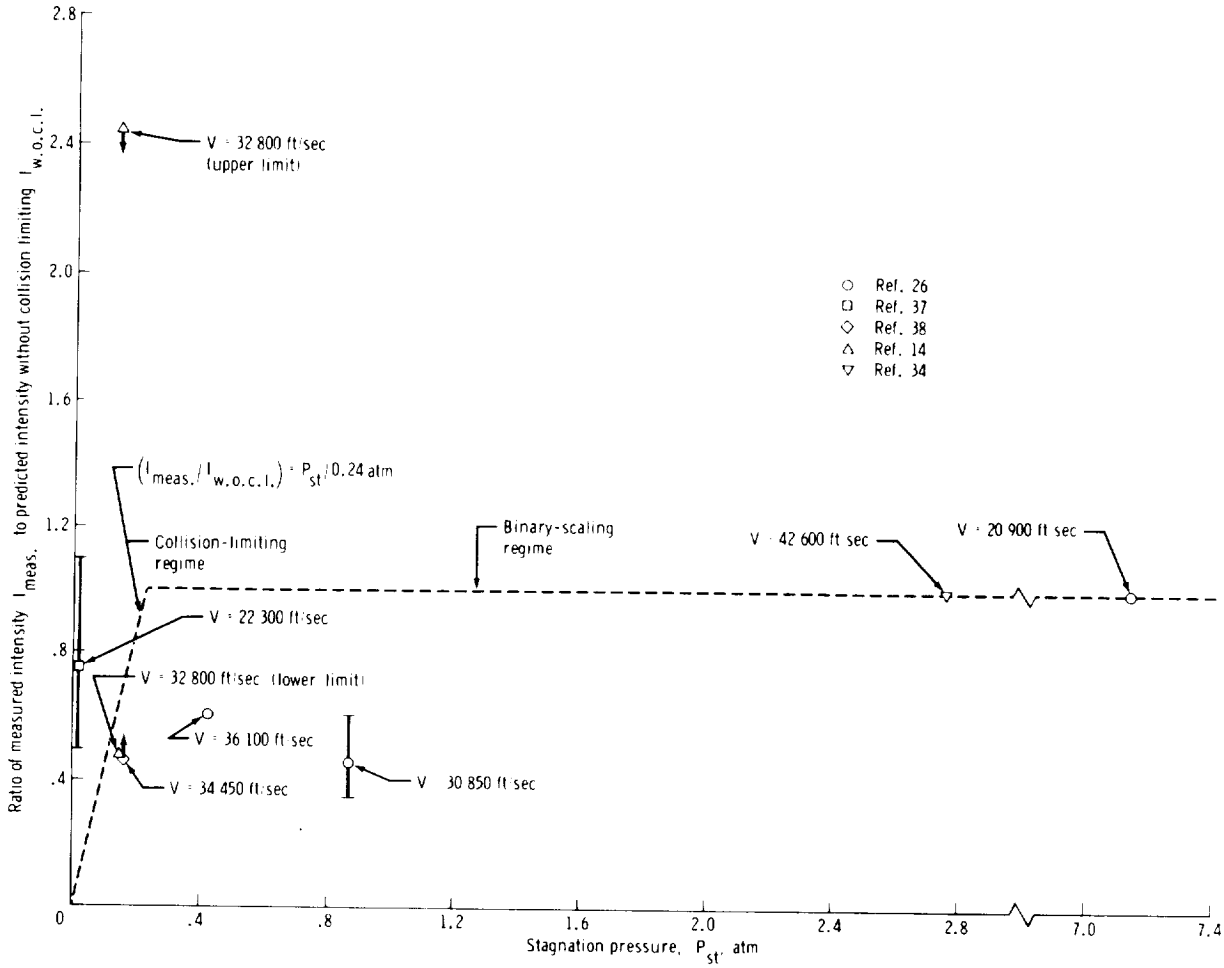

Figure 12. - Comparison of collision-limiting approximation with measured nonequilibrium radiant intensity.

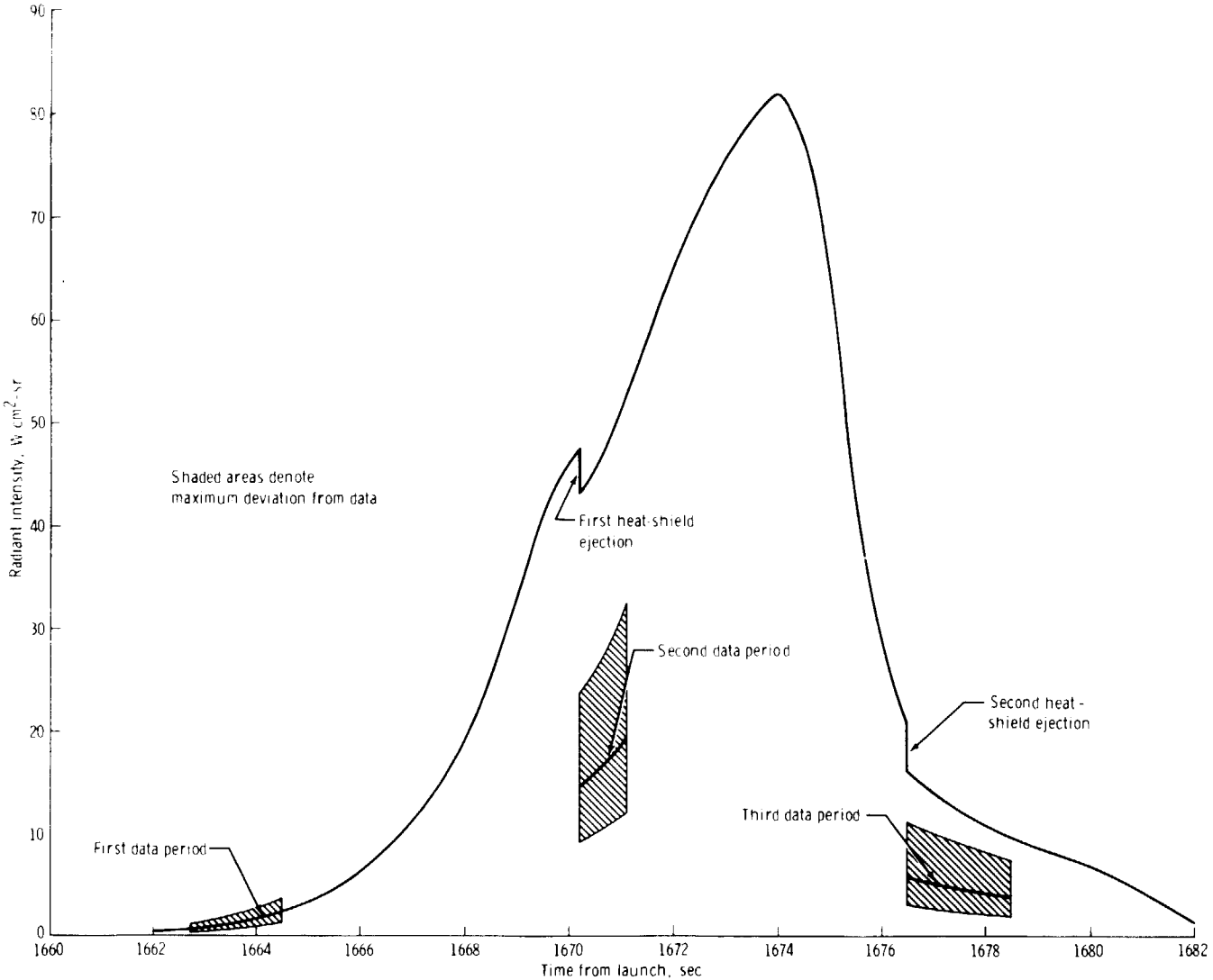

(a) FIRE I.

Figure 13. - Comparison of predicted radiant intensity with measured radiometer data for FIRE I and FIRE II trajectories.

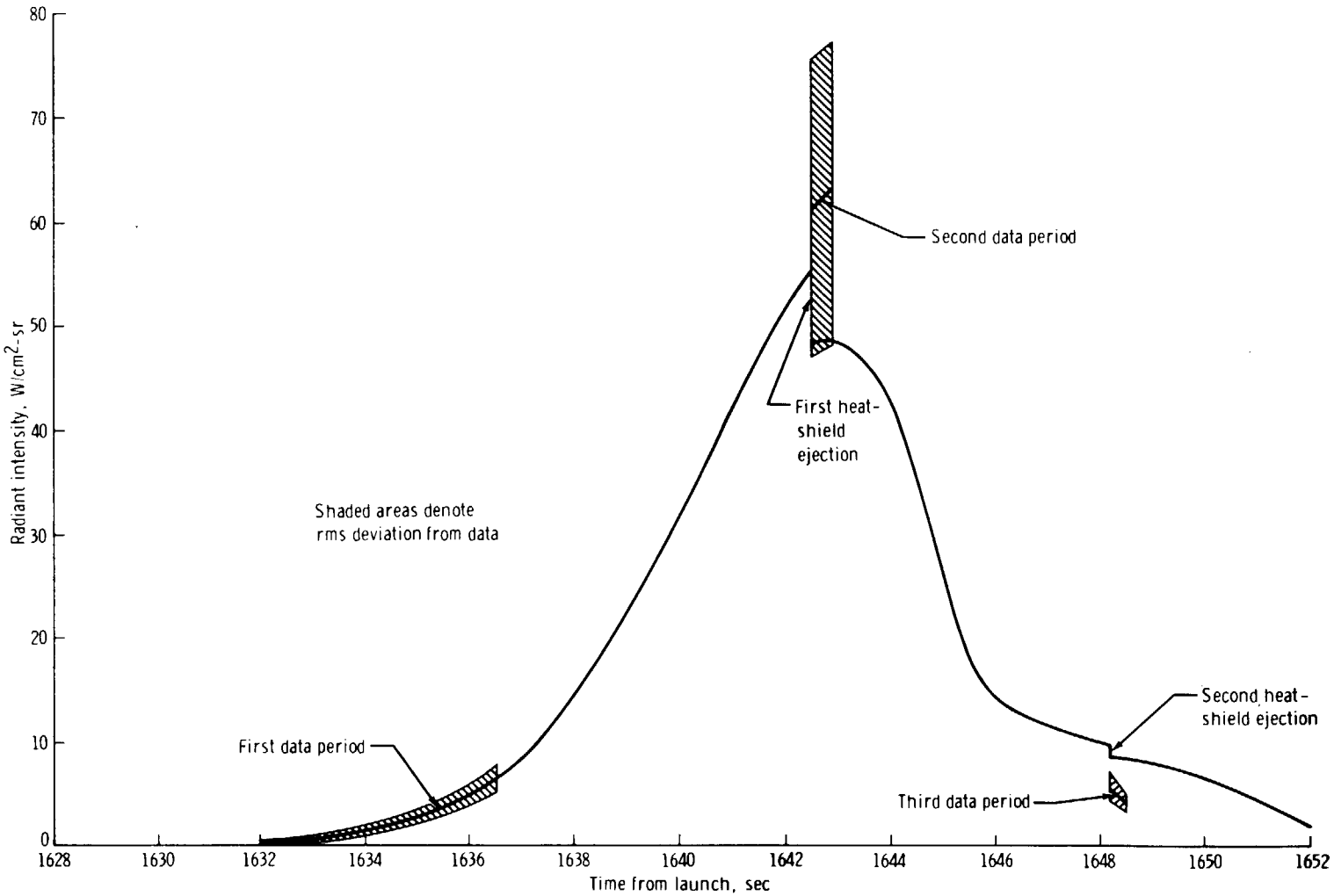

(b) FIRE II.

Figure 13. - Concluded.

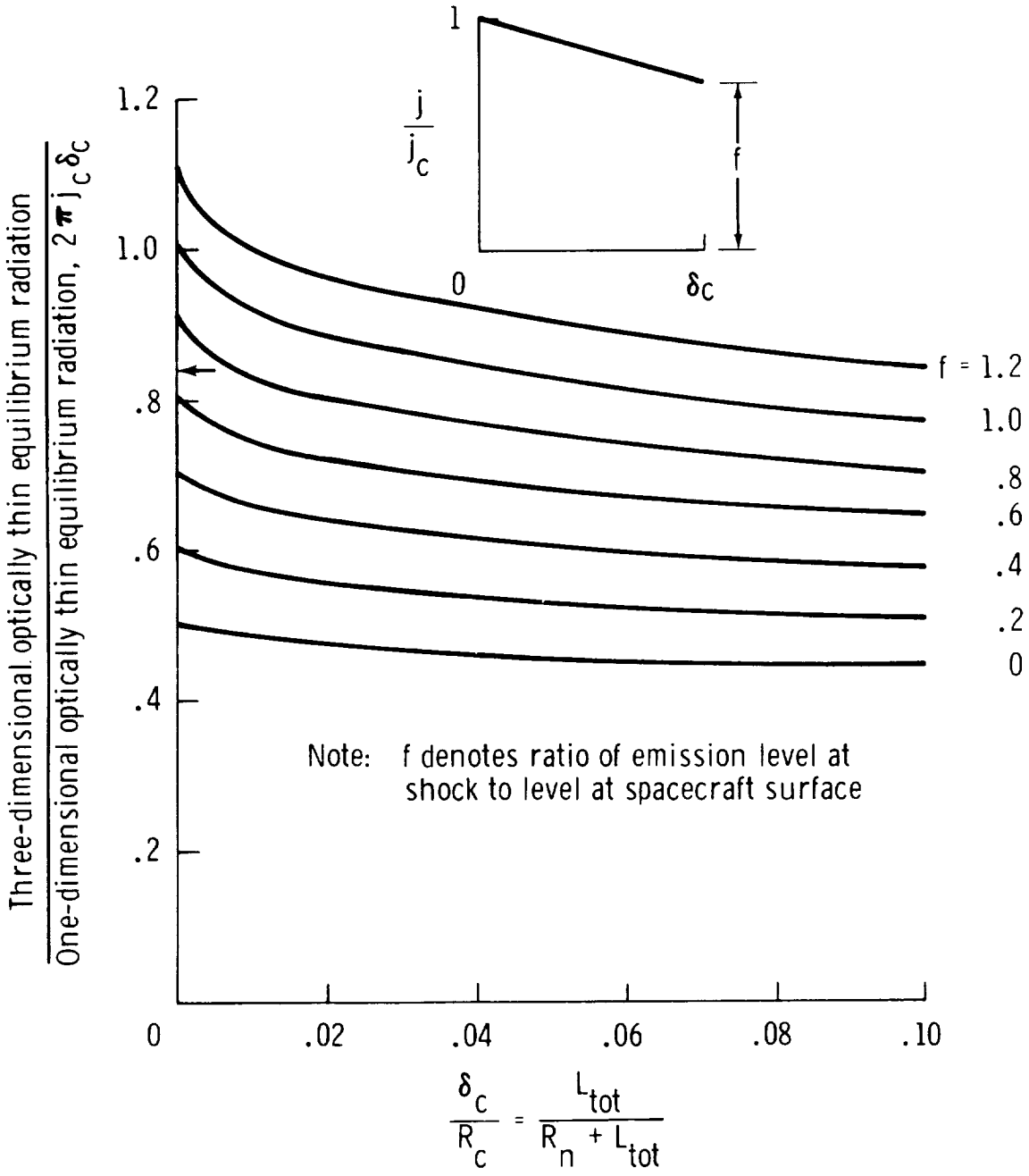

Figure 14. - Thin-gas radiative heat flux from a spherical segment of radius R_c and thickness δ_c compared to the infinite plane-slab approximation.

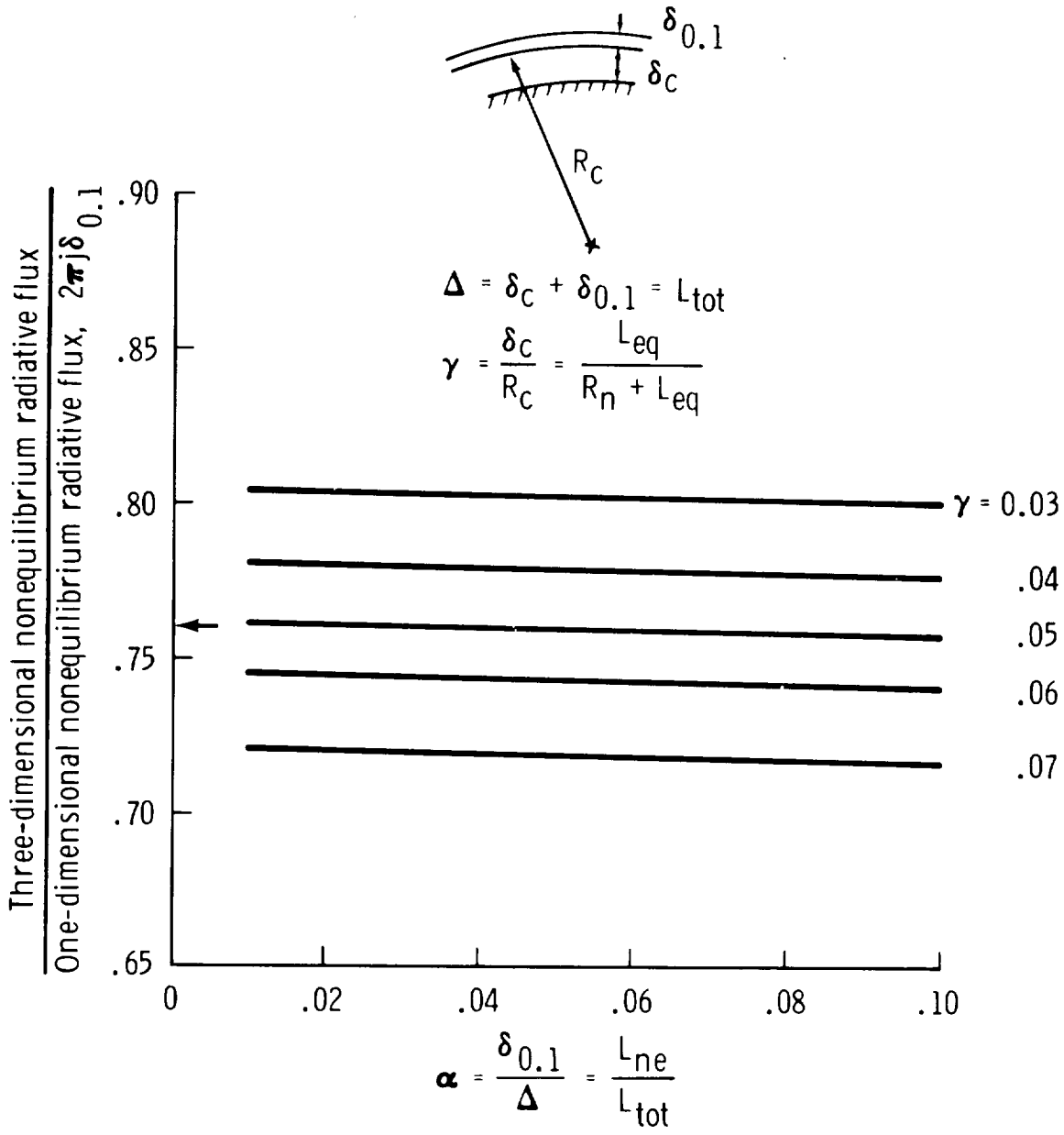

Figure 15. - Nonequilibrium radiative heating rate for the concentric-spheres approximation compared to the infinite plane-slab approximation.

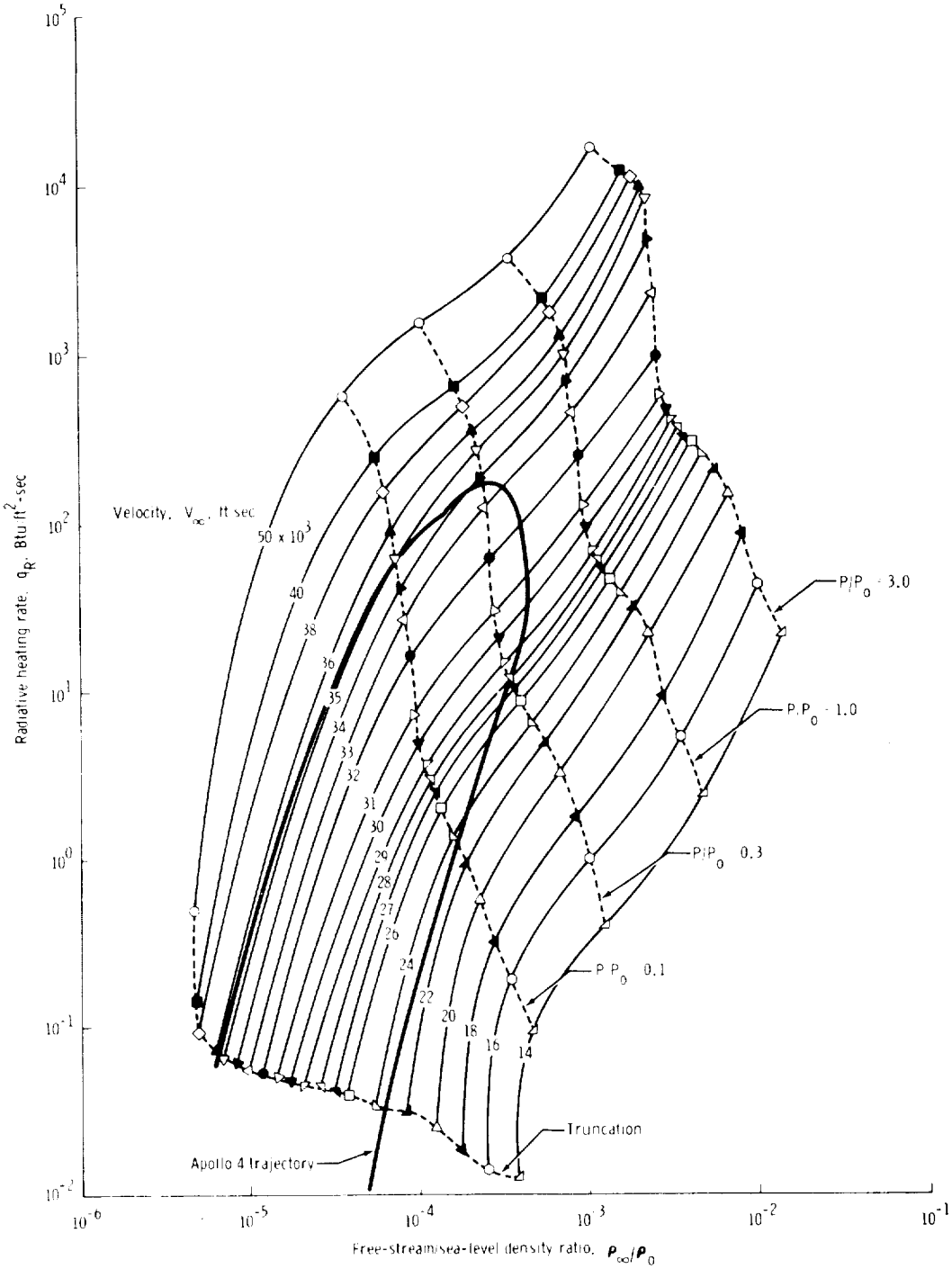

Figure 16. - Radiative heating rate as a function of density ratio and velocity for the Apollo command module at S/R = 0.732 for a 24.4° angle of attack.

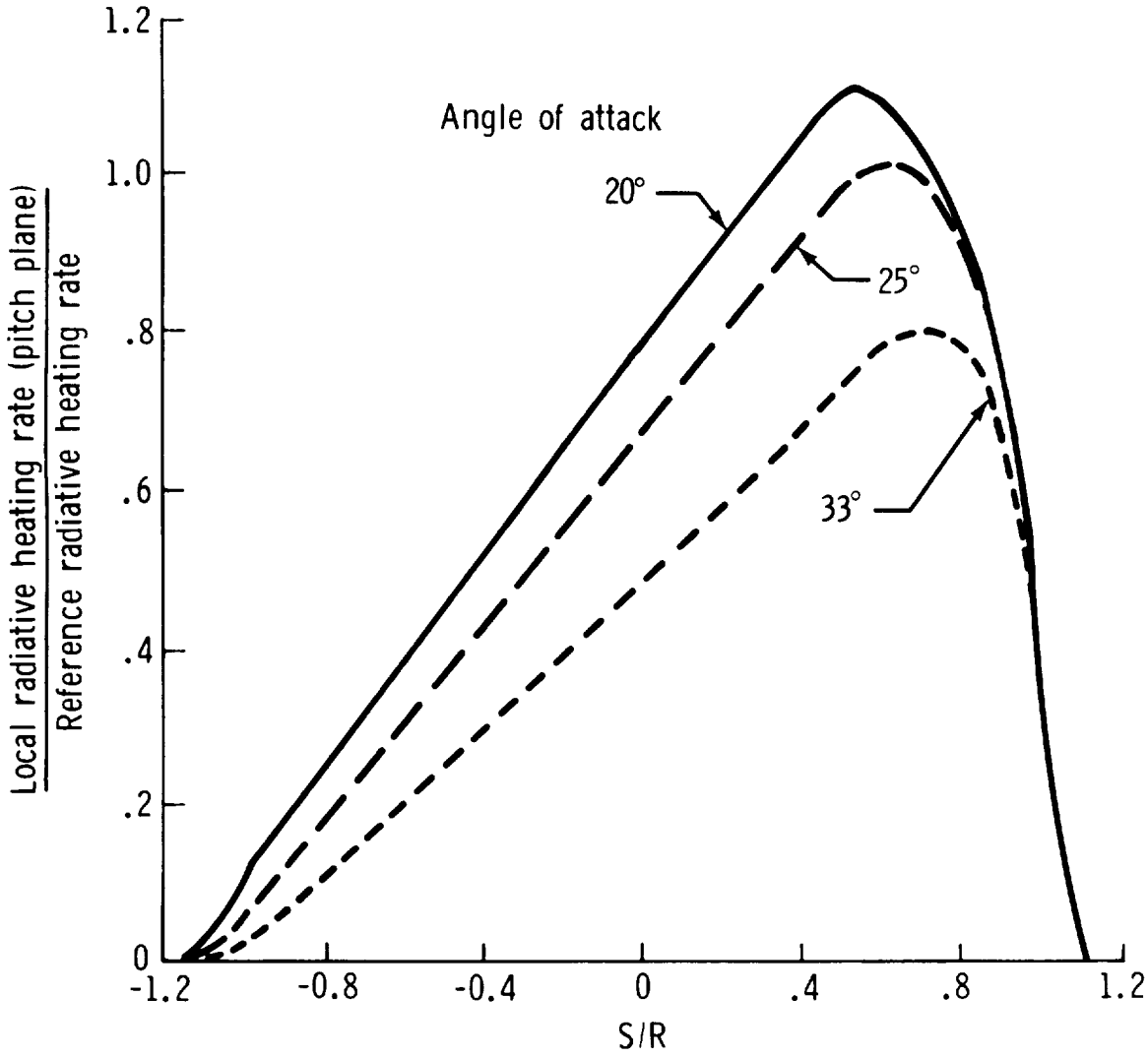

(a) Along the pitch plane.

Figure 17. - Radiative heating distribution of the Apollo command module as a function of angle of attack.

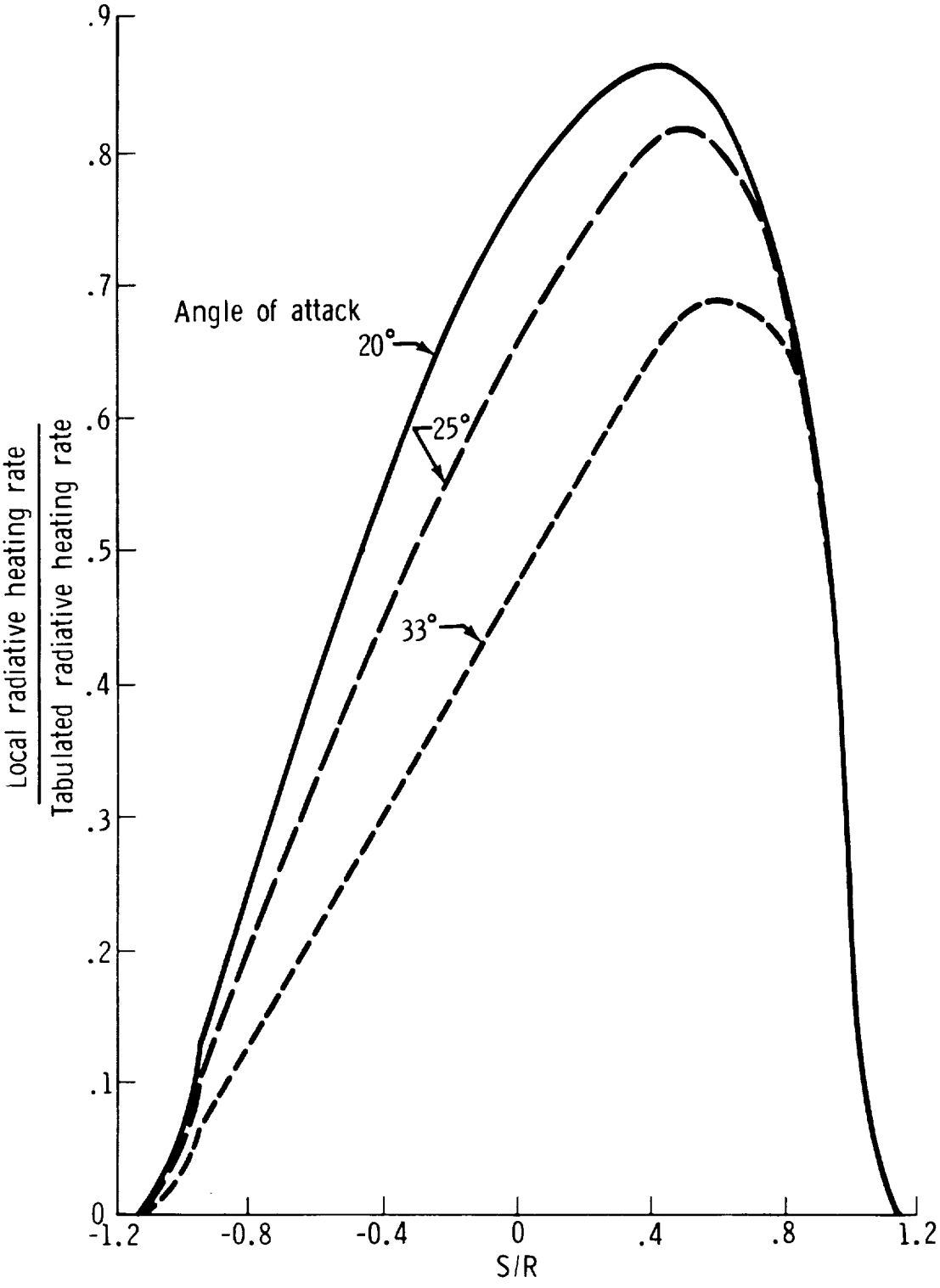

(b) At 45° from the pitch plane.

Figure 17. - Continued.

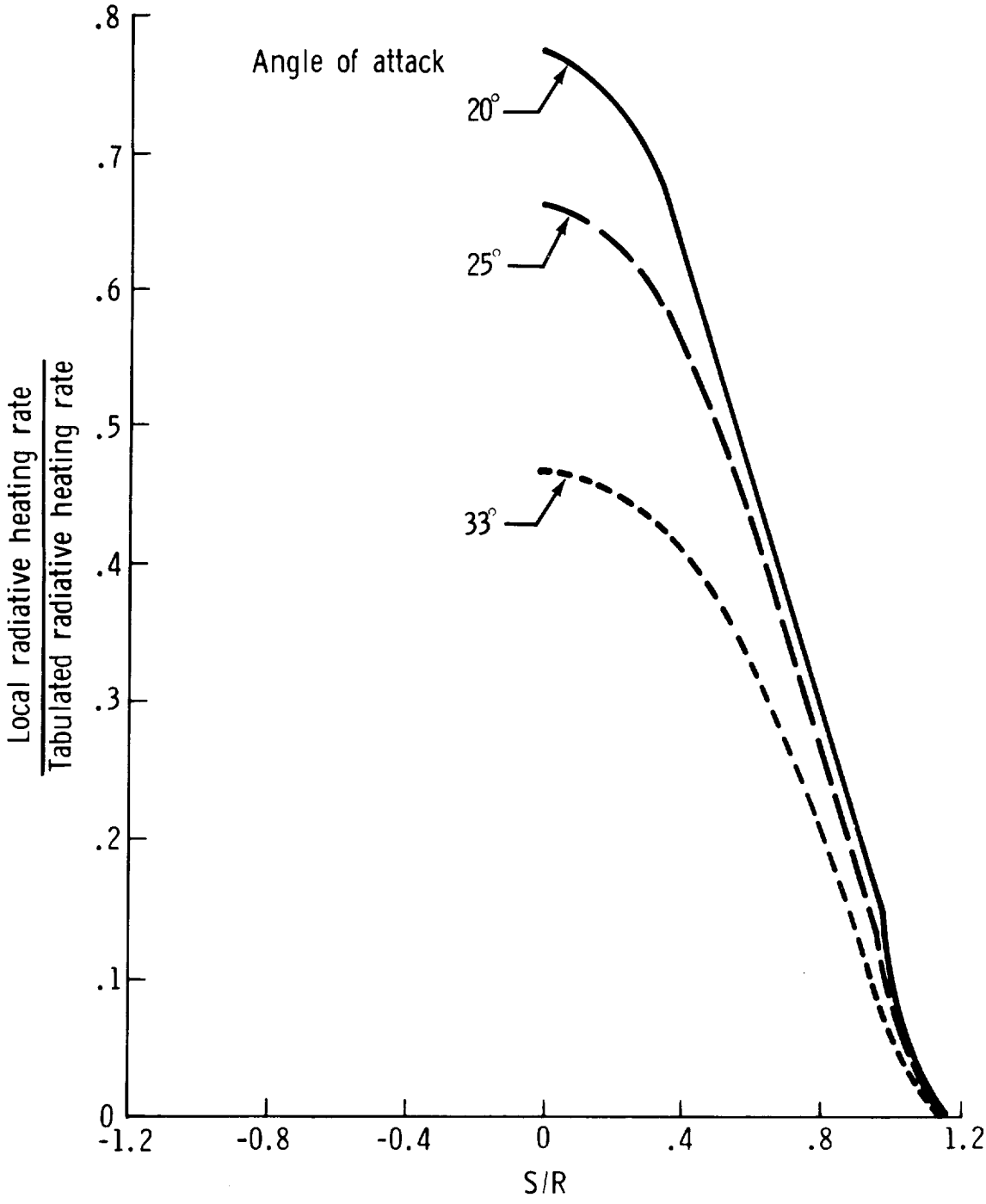

(c) Along the yaw plane.

Figure 17. - Concluded.

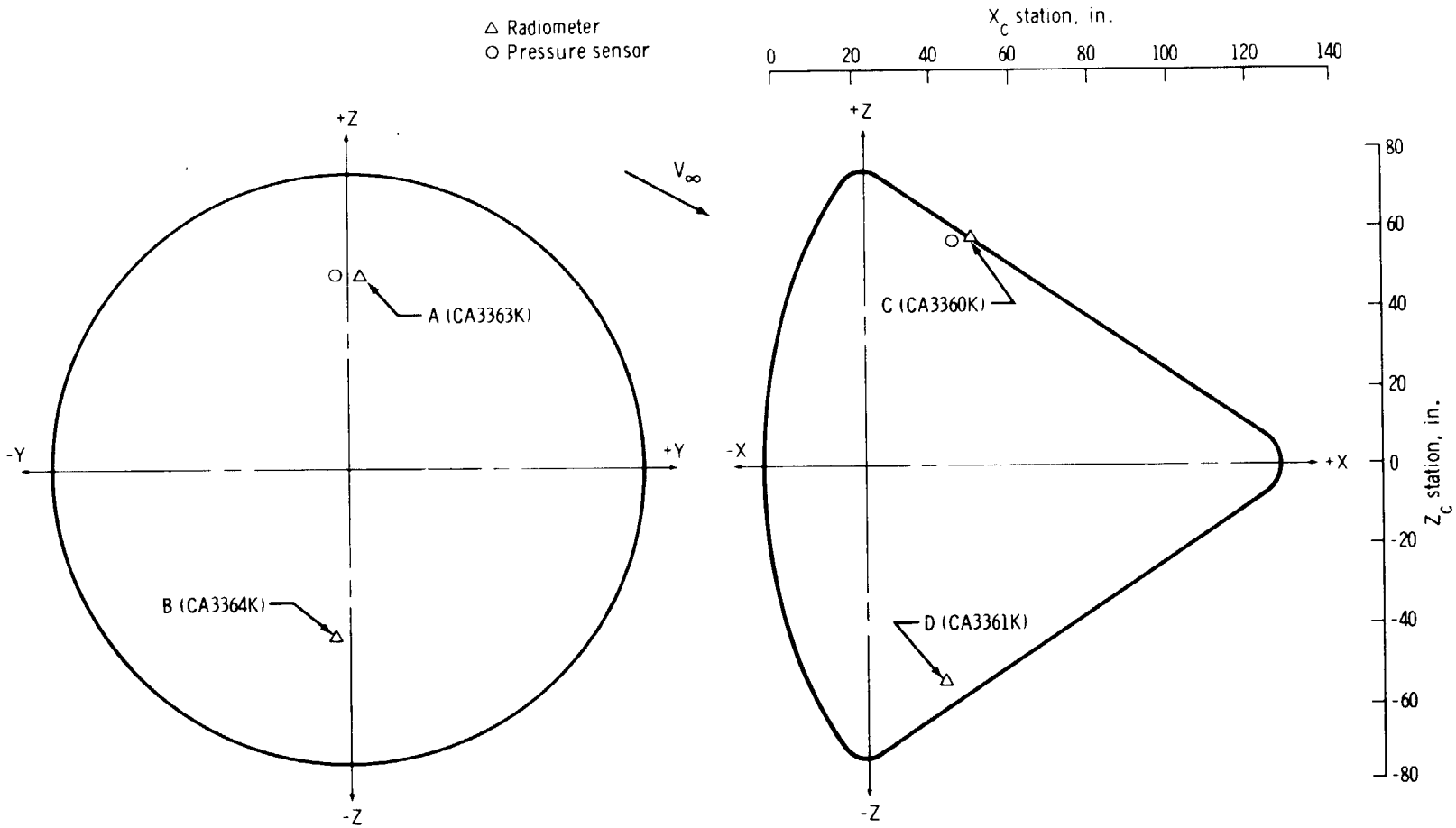

Figure 18. - Apollo 4 radiometer and stagnation-pressure transducer locations.

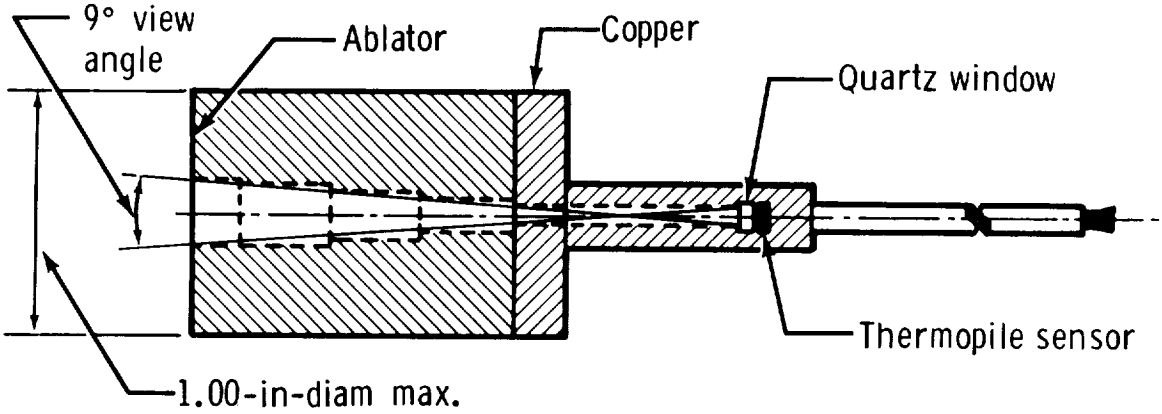

Figure 19. - Sketch of radiometer.

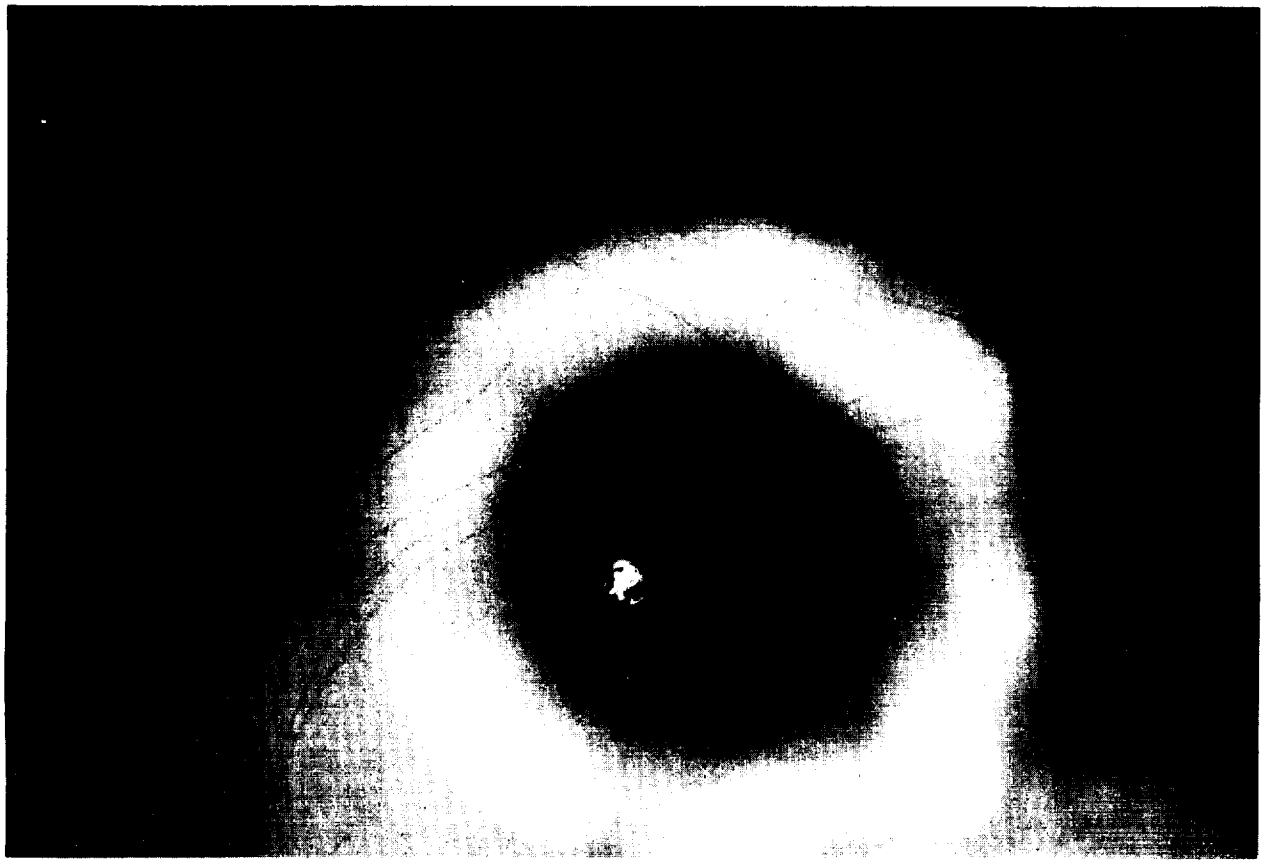

Figure 20. - Photograph, showing quartz window, of CA3363K radiometer after flight.

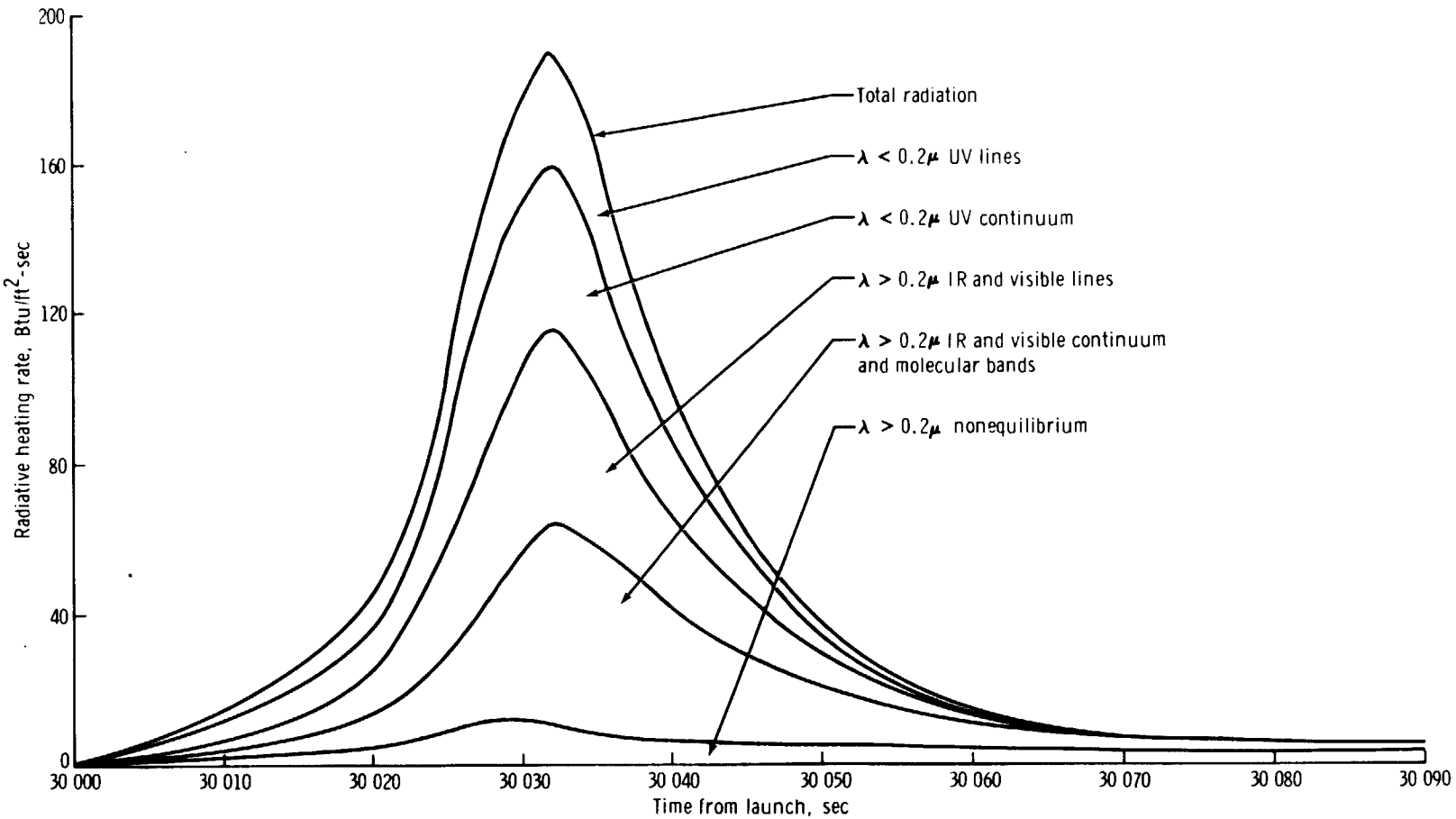

Figure 21. - Components of Apollo 4 radiative heating rate near the stagnation point.

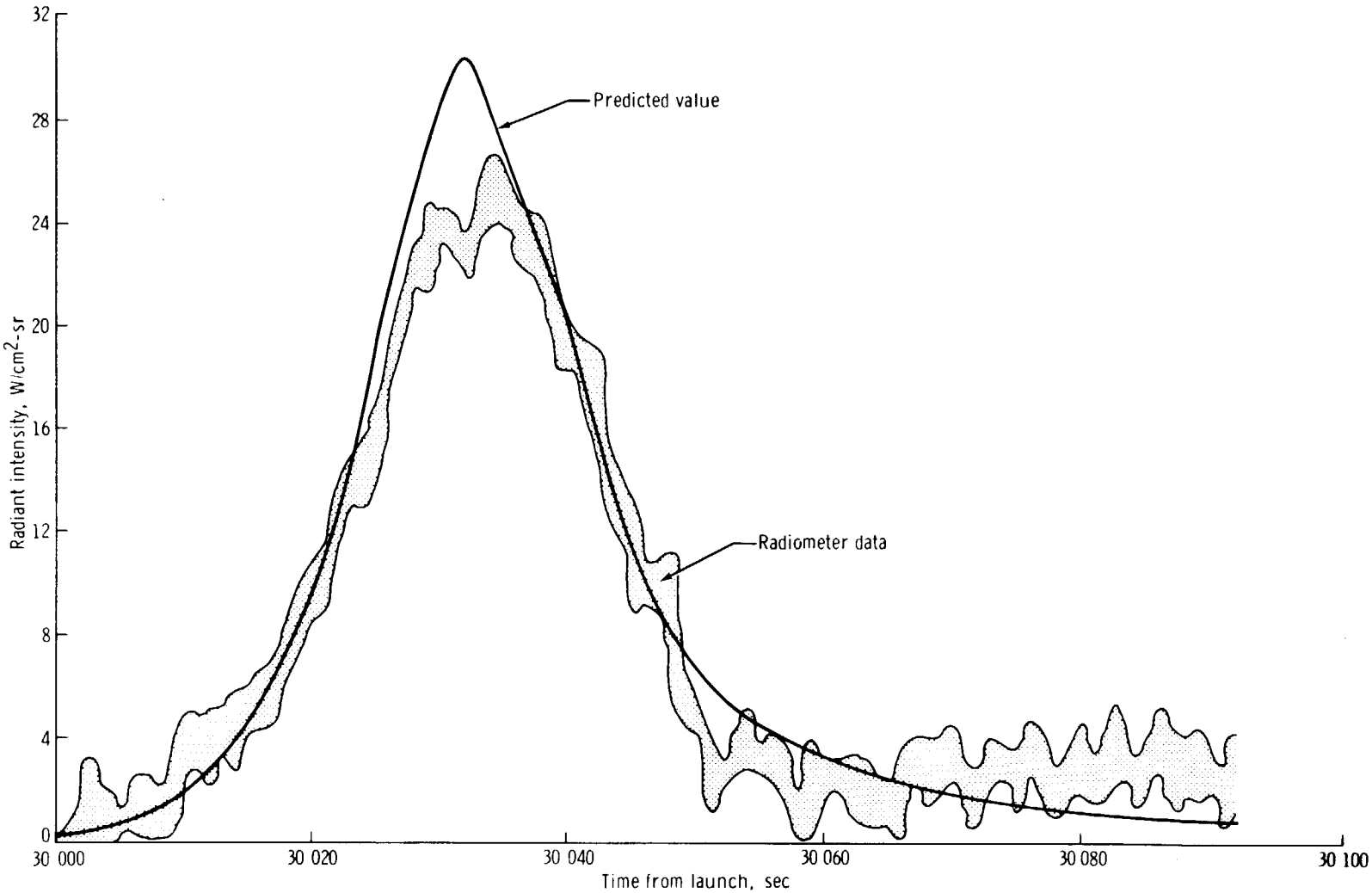

Figure 22. - Comparison of radiant-intensity predictions with Apollo 4 radiometer flight data.

APPENDIX A

COMPUTER PROGRAM FOR PREDICTION OF RADIATIVE HEATING TO THE APOLLO COMMAND MODULE

The technique of predicting radiation heating from the shock front to the Apollo CM as described in the section on radiative heating was automated such that, for a particular trajectory, the radiation heating rate to any point on the CM could be calculated easily. Basically, this computer program for predicting radiation heating (designated QRAD) involves the use of the four-band equilibrium radiation model of the NASA Ames Research Center (ref. 16) and the use of several figures in this report pertaining to the nonequilibrium radiation, shock-standoff distances, three-dimensional and nonadiabatic factors, and so forth.

The four-band equilibrium radiation model includes radiation from (1) infrared lines (223 N and O atomic lines) in the wavelength range $0.395\mu < \lambda < 1.316\mu$, (2) visible continuum (free-free and free-bound processes involving N and O atoms and N^- and O^- ions) in the region $0.113\mu < \lambda < \infty$, (3) ultraviolet lines (47 N and O atomic lines) in the range $0.110\mu < \lambda < 0.175\mu$, and (4) ultraviolet continuum (N and O free-bound processes) in the wavelength region $0 < \lambda < 0.113\mu$. The molecular radiation is included with the continuum band models, and the visible lines are included in the infrared band model.

The original radiative properties tabulated in reference 16 were plotted in a form convenient to use with trajectories. The following quantities were plotted as a function of the stagnation/sea-level pressure ratio P_{st}/P_o and the stagnation enthalpy h_{st} (or stagnation temperature T_{st}).

1. $\alpha_{\text{vis. cont.}}$ mean absorption coefficient for the visible continuum
2. $\alpha_{\text{IR lines}}$ mean absorption coefficient for the infrared lines
3. $\alpha_{\text{UV cont.}}$ mean absorption coefficient for the ultraviolet continuum
4. $\overline{B}_{\text{vis. cont.}}$ integrated black-body intensity for the visible continuum
5. $\overline{B}_{\text{IR lines}}$ integrated black-body intensity for the infrared lines
6. $\overline{B}_{\text{UV cont.}}$ integrated black-body intensity for the ultraviolet continuum
7. $B_{\lambda,o}\omega/\sqrt{L_{eq}}$ parameter for the ultraviolet lines

For a particular trajectory, the quantities of time, altitude, density, stagnation enthalpy, pressure ratio, and nose radius are input for each point in the computer program. The absorption coefficients and black-body intensities are curve fitted for various pressure ratios as a function of stagnation enthalpy. A semilogarithmic interpolation technique is provided in the program to interpolate between pressure ratios. A linear or five-point Lagrangian technique is used for the interpolation of most of the other parameters that were curve fitted in the program.

The total shock-standoff distance/nose-radius ratio L_{tot}/R_n and the nonequilibrium relaxation distance L_{ne} are obtained as a function of velocity and altitude from figures 5 and 7 (curve fitted into the program). Then, the equilibrium shock-standoff distance is calculated as

$$L_{eq} = \left(L_{tot}/R_n\right)R_n - L_{ne} \tag{1}$$

where the radius for the Apollo CM is taken to be 10 feet for an angle of attack of 24.4°.

The radiative heating from the shock front to the CM then is calculated by assuming the shock front (gas cap) to be an isothermal slab (one-dimensional plane). For this assumption, the radiation from the infrared lines, visible continuum, and ultraviolet continuum is calculated, respectively, as

$$q_{\text{IR lines}} = 2\pi(0.88)\overline{B}_{\text{IR lines}}\left[0.5 - E_3\left(\alpha_{\text{IR lines}}L_{eq}\right)\right] \tag{2}$$

$$q_{\text{vis. cont.}} = 2\pi(0.88)\overline{B}_{\text{vis. cont.}}\left[0.5 - E_3\left(\alpha_{\text{IR lines}}L_{eq}\right)\right] \tag{3}$$

$$q_{\text{UV cont.}} = 2\pi(0.88)\overline{B}_{\text{UV cont.}}\left[0.5 - E_3\left(\alpha_{\text{UV lines}}L_{eq}\right)\right] \tag{4}$$

where $E_3(\alpha L)$ is the integro-exponential functional of the third order and the integrated black-body intensity $\overline{B}$ is defined as

$$\overline{B} = \int_{\nu_1}^{\nu_2} B_\nu \, d\nu \tag{5}$$

where ν is the wave number.

For the ultraviolet lines, the heating rate is calculated as

$$q_{UV\ lines} = (4/3)\pi(0.88)B_{\lambda,o}\left(\omega/\sqrt{L_{eq}}\right)\sqrt{L_{eq}} \tag{6}$$

All these relations for radiative heating rates have units of Btu/ft^2-sec. The radiative intensities that have units of W/cm^2 are also calculated in the program as

$$I_{IR\ lines} = \overline{B}_{IR\ lines}\left[1 - \exp\left(-\alpha_{IR\ lines} L_{eq}\right)\right] \tag{7}$$

$$I_{vis.\ cont.} = \overline{B}_{vis.\ cont.}\left[1 - \exp\left(-\alpha_{vis.\ cont.} L_{eq}\right)\right] \tag{8}$$

$$I_{UV\ cont.} = \overline{B}_{UV\ cont.}\left[1 - \exp\left(-\alpha_{UV\ cont.} L_{eq}\right)\right] \tag{9}$$

and

$$I_{UV\ lines} = B_{\lambda,o}\left(\omega/\sqrt{L_{eq}}\right)\sqrt{L_{eq}} \tag{10}$$

The equilibrium radiation heating rate for a one-dimensional slab with no radiative cooling (adiabatic flow) $q_{1\text{-}d,\,adia}$ is calculated thus as

$$q_{eq,\,1\text{-}d,\,adia} = q_{IR\ lines} + q_{vis.\ cont.} + q_{UV\ cont.} + q_{UV\ lines} \tag{11}$$

The nonequilibrium radiation for a one-dimensional isothermal slab with no radiation cooling is obtained from the relation

$$q_{ne,\,1\text{-}d,\,adia} = 2\pi(0.88)I_{ne}\left(\frac{P_{st}/P_o}{0.24}\right) \tag{12}$$

where I_{ne} is the nonequilibrium intensity for binary scaling obtained from interpolating on the middle curve of figure 11 plotted as a function of flight velocity. The factor in parentheses in equation (12) is a linear collision-limiting factor that is based on experimental data (fig. 13) and that is set equal to 1 for pressures higher than 0.24 atmosphere.

A three-dimensional shock curvature factor for equilibrium radiation $F_{eq, 3\text{-}d}$ is obtained as a function of $L_{tot}/(R_n + L_{tot})$ from figure 14. Also, a three-dimensional factor for nonequilibrium radiation $F_{ne, 3\text{-}d}$ is taken as a function of L_{ne}/L_{tot} and $L_{eq}/(R_n + L_{eq})$ from figure 15. The factors from both of these figures are curve fitted in the program.

Hence, the total radiation for three-dimensional adiabatic flow is calculated as

$$q_{tot, 3\text{-}d, adia} = q_{eq, 1\text{-}d, adia}\left(F_{eq, 3\text{-}d}\right) + q_{ne, 1\text{-}d, adia}\left(F_{ne, 3\text{-}d}\right) \tag{13}$$

A nonadiabatic (radiative cooling) factor q_{na}/q_{adia} is obtained by interpolation from curves of q_{na}/q_{adia} as a function of the free-stream/sea-level density ratio ρ_∞/ρ_0 and the flight velocity V_∞. These curves are shown in figure 10(a) for the visible continuum, infrared lines, and nonequilibrium radiation and in figure 10(b) for the ultraviolet lines and ultraviolet continuum.

The heating rate received by the radiometer is the sum of the visible and infrared equilibrium components and the nonequilibrium component and is calculated as

$$q_{rdmtr} = F_{eq, 3\text{-}d}\left(q_{vis.\ cont.} + q_{IR\ lines}\right) + F_{ne, 3\text{-}d} q_{ne, 1\text{-}d, adia}\left(q_{na}/q_{adia}\right)_{vis., IR, ne} \tag{14}$$

The final expression for total radiation for three-dimensional nonadiabatic flow is calculated thus as

$$q_{tot, 3\text{-}d, na} = q_{rdmtr} + F_{eq, 3\text{-}d}\left(q_{UV\ lines} + q_{UV\ cont.}\right)\left(q_{na}/q_{adia}\right)_{UV} \tag{15}$$

A sample output sheet for one point in the Apollo 4 trajectory is shown in figure A-1. The final value of $q_{tot, 3\text{-}d}$ of 178 Btu/ft^2-sec compares very closely with that read off the chart in figure 16. This figure shows the latest operational heating rates for the Apollo CM with a 10-foot radius at an angle of attack of 24.4°, and for S/R = 0.732, the approximate location of the Apollo 4 radiometer CA3363K. For other angles of attack and values of S/R, the curves of figure 17 are used.

In summary, this computer program is believed to provide a satisfactory technique for predicting radiative heating to vehicles entering the earth atmosphere. These vehicles include the Apollo 4 CM (fig. 22), FIRE I and FIRE II (fig. 13), and the lunar module and Saturn IVB stage.

```
      CASE  200, AS-501 TRAJECTORY

PROBLEM NUMBER 12

   TIME= 0.30030E 05    VEL= 0.33850E 05     ALT= 0.19080E 06     DENSITY= 0.18200E-04
       STAGNATION ENTHALPY= 0.22850E 05     PRESSURE RATIO= 0.30000E 00
       NOSE RADIUS= 0.30500E 03


   ALPHA   VIS   CONT      =     0.43180E-04    Average absorption coefficient for visible continuum
   ALPHA   UV    CONT      =     0.13315E 00    Average absorption coefficient for ultraviolet continuum
   ALPHA   IR    LINE      =     0.65223E-01    Average absorption coefficient for infrared lines
   B       VIS   CONT      =     0.20309E 05    Integrated blackbody intensity for visible continuum
   B       UV    CONT      =     0.38268E 0E    Integrated blackbody intensity for ultraviolet continuum
   B       IR    LINE      =     0.32750E 02    Integrated blackbody intensity for infrared lines
   BW/L    UV    LINE      =     0.42512E 01    Parameter for ultraviolet lines
   L-TOTAL                 =     0.15165E 02    Total shock stand-off distance
   L-EQ                    =     0.14738E 02    Equilibrium shock stand-off distance
   L-NON EQ                =     0.42722E 00    Nonequilibrium shock stand-off (relaxation) distance
   Q-VIS   CONT            =     0.67891E 02    Radiative heating rate for 1-d adiabatic flow for visible continuum
   Q-IR    LINE            =     0.69500E 02    Radiative heating rate for 1-d adiabatic flow for infrared lines
   Q-UV    CONT            =     0.98958E 02    Radiative heating rate for 1-d adiabatic flow for ultraviolet continuum
   Q-UV    LINE            =     0.60162E 02    Radiative heating rate for 1-d adiabatic flow for ultraviolet lines
   I-VIS   CONT            =     0.12921E 02    Radiative intensity for 1-d adiabatic flow for visible continuum
   I-UV    CONT            =     0.32890E 02    Radiative intensity for 1-d adiabatic flow for ultraviolet continuum
   I-IR    LINE            =     0.20226E 02    Radiative intensity for 1-d adiabatic flow for infrared lines
   I-UV    LINE            =     0.16321E 02    Radiative intensity for 1-d adiabatic flow for ultraviolet lines
   I-NON EQ                =     0.31948E 01    Nonequilibrium intensity for 1-d adiabatic flow
   I-RDMTR NON AD          =     0.29926E 02    Radiometer intensity (vis. + ir + ne) for 1-d nonadiabatic flow
   I-TOTAL NON AD          =     0.56884E 02    Total intensity (vis. + ir + ne + uv) for 1-d nonadiabatic flow
   COEF                    =     0.10000E 01    Collision limiting coefficient
   Q-NON EQ                =     0.17665E 02    Nonequilibrium heating rate for 1-d adiabatic flow
   Q-EQ                    =     0.29651E 03    Equilibrium heating rate (vis. + ir + uv) for 1-d adiabatic flow
   F-NON EQ 3D             =     0.76829E 00    Nonequilibrium 3-d factor
   F-EQ 3D                 =     0.83386E 00    Equilibrium 3-d factor
   F-NON AD VIS-IR         =     0.82345E 00    Nonadiabatic factor for visible and infrared (incl. noneq.) radiation
   F-NON AD UV             =     0.54782E 00    Nonadiabatic factor for ultraviolet radiation
   Q-TOTAL 3D AD           =     0.26082E 03    Total radiative heating rate (vis. + ir + ne + uv) for 3-d adiabatic flow
   Q-RDMTR NON AD          =     0.10551E 03    Radiometer heating rate (vis. + ir + ne) for 3-d nonadiabatic flow
   Q-TOTAL 3D NON AD       =     0.17820E 03    Total heating rate (vis. + ir + ne + uv) for 3-d nonadiabatic flow
```

Figure A-1. - Sample output sheet from the radiative heating rate program (QRAD).

APPENDIX B

POSTFLIGHT RADIOMETER PERFORMANCE TESTS

The radiometer data presented in the section on flight measurement were obtained through the direct application of a preflight calibration of the radiometer instrument. However, the flight data are affected by processes in the ablator cavity, and the instrument response is affected by the instrument mounting in the ablation heat shield. It was believed that the best way to account for these effects was through an experimental simulation of the local heating-rate history both with ablator cavity models and with the flight-instrument configuration. As shown in figure 22, the flight-radiometer data fell below the predicted radiative heating by approximately 20 percent, and, after the peak in the radiative heating history, the radiative data tended to drift relative to the prediction. In addition, a postflight inspection of the radiometer revealed a residue on the protective quartz window.

Tests were performed in the MSC 1.5-megawatt entry-materials evaluation facility to investigate these discrepancies. The test models were subjected to the heat pulses shown superimposed over the Apollo 4 heating rate history in figure B-1. Three basic model configurations were employed: 4-inch-diameter ablating models, 2-inch-diameter ablating models, and 2-inch-diameter water-cooled models.

The purpose of the 4-inch-diameter models was to determine the approximate time that the deposits were formed in the flight-radiometer cavities. Each model contained four heating-rate sensors mounted at the bottoms of four holes that simulated the radiometer viewing holes used on the Apollo 4 spacecraft. A sketch of the 4-inch-diameter hole model is shown in figure B-2. Post-test views of the hole models and of the simulated radiometer bodies are shown in figures B-3 and B-4, respectively. Although post-test inspections of these radiometer bodies revealed tarlike deposits on the exteriors, no deposits were found within the viewing holes. The deposit resulted from a flow of hot gas through the model after the failure of a gas seal in the rear of the model. In addition, there was no reduction in the output of the heating rate sensors during the tests; this also is suggestive that the deposits were lodged in the flight-radiometer cavities by aerodynamic forces after peak heating had occurred.

The purpose of the 2-inch-diameter radiometer models was to gage the performance characteristics of the flight-type radiometer under simulated entry conditions. The radiometer models were constructed of Apollo ablator material and contained one radiometer each. Four other radiometers were tested in a water-cooled model (fig. B-5) that had the same configuration as the radiometer models. A post-test view of an ablator-type radiometer model is shown in figure B-6.

During the tests, the radiometer models were subject not only to the convective heating of the supersonic test stream but also were exposed to radiative heating from the end of a constricted electric arc. The arc column provided a constant reference level of intense radiation during the tests. Any changes in the radiometer output would be characteristic of the instruments. Referring to figure 22, it can be seen that a prominent dip in the radiometer data occurred at 30 032 seconds from launch. This same phenomenon was observed for the ablator-type radiometer models but not for the cooled models, as shown in figure B-7. This decrease is apparently caused by the

attenuation of the infrared wavelengths during the temporary formation of relatively cool ablation products within the radiometer cavities. Once the cavity warms, the attenuation decreases and the radiometer reaches its peak value. It is probable that the same effect causes the flight data in figure 22 to dip below the predicted values just before the peak in radiant heating.

In addition, the radiometers tested in the arc-jet facility exhibited a drift behavior when mounted in an ablator-type holder but behaved normally when mounted in a water-cooled holder, as shown in figure B-7. This phenomenon is the result of a changing radiometer-body temperature that subsequently changes the thermopile heat flux. A correlation between the nearest indepth thermocouple response and the difference between the flight-radiometer data and the predictions can be seen in figure B-8. Thus, this discrepancy between the flight data and the predictions is most likely because of the temperature excursions of the ablator material surrounding the radiometer body.

Although the ground test could not provide sufficient information to correct quantitatively the flight data for the instrument performance in the ablator mounting, it appears qualitatively that the differences between the flight data and the engineering predictions are attributable to the measurement phenomenon observed in the ground simulation. It is suggested that radiometers mounted in heat shields in the future be designed to minimize changes in body temperature, to compensate automatically for temperature changes, or to record body temperature.

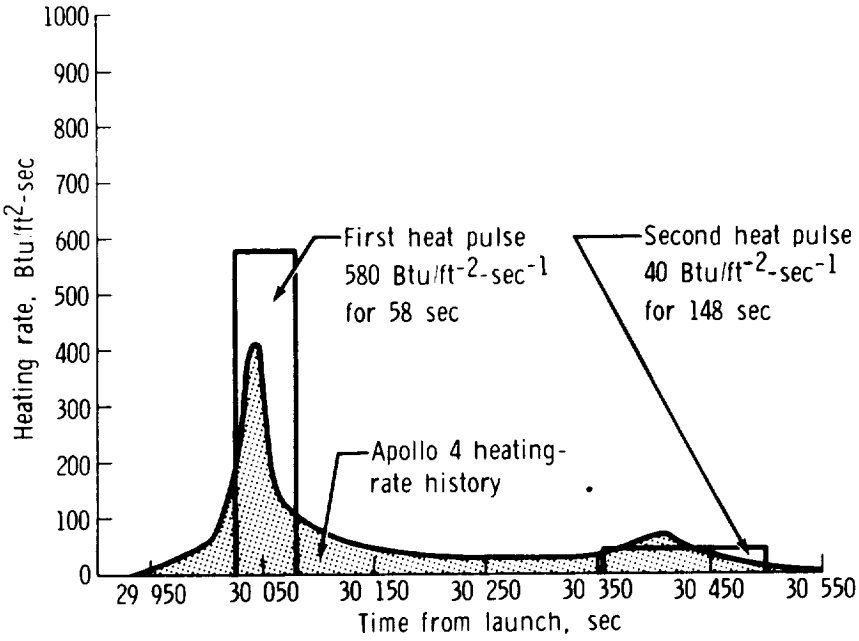

Figure B-1. - Radiometer model test conditions.

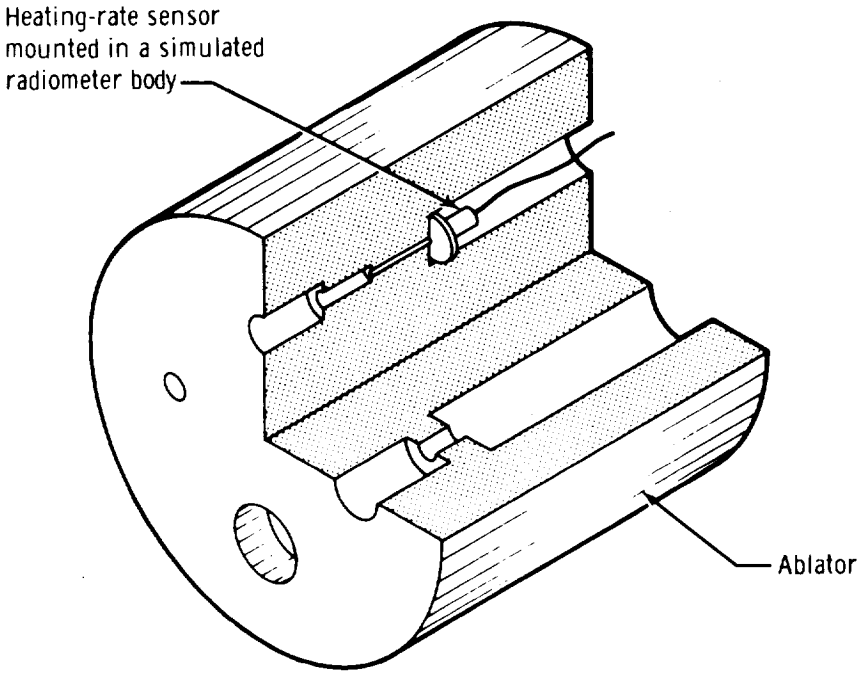

Figure B-2. - Sketch of radiometer hole model.

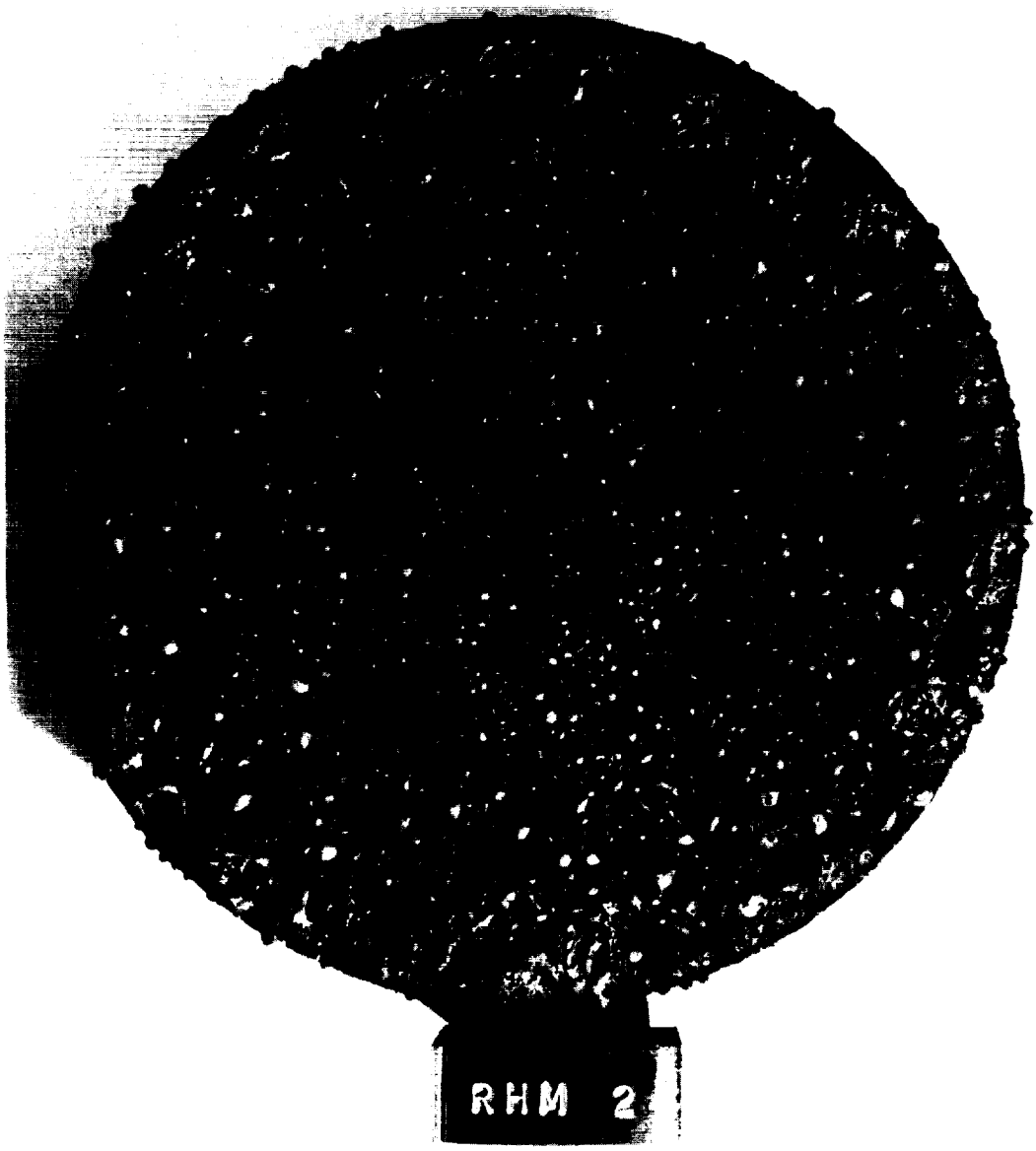

Figure B-3. - Post-test view of radiometer hole model.

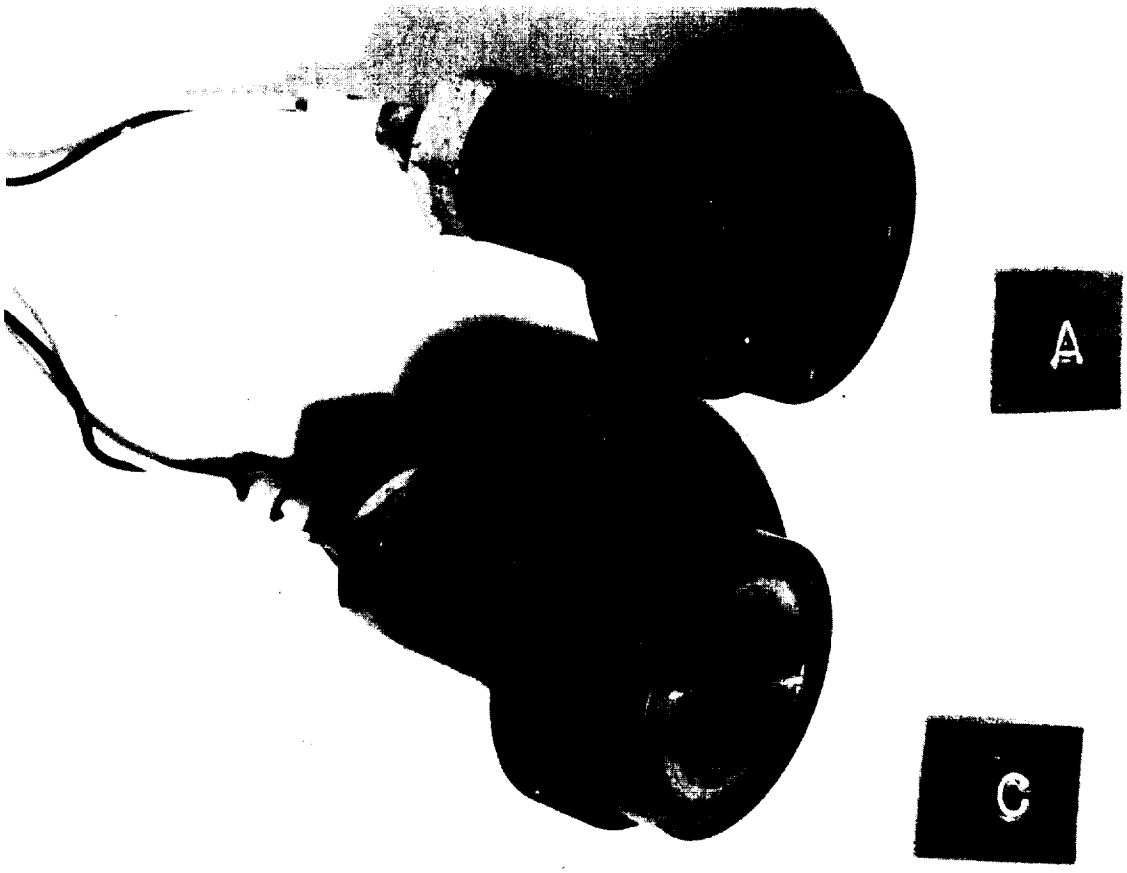

Figure B-4. - Post-test views of the simulated radiometer bodies.

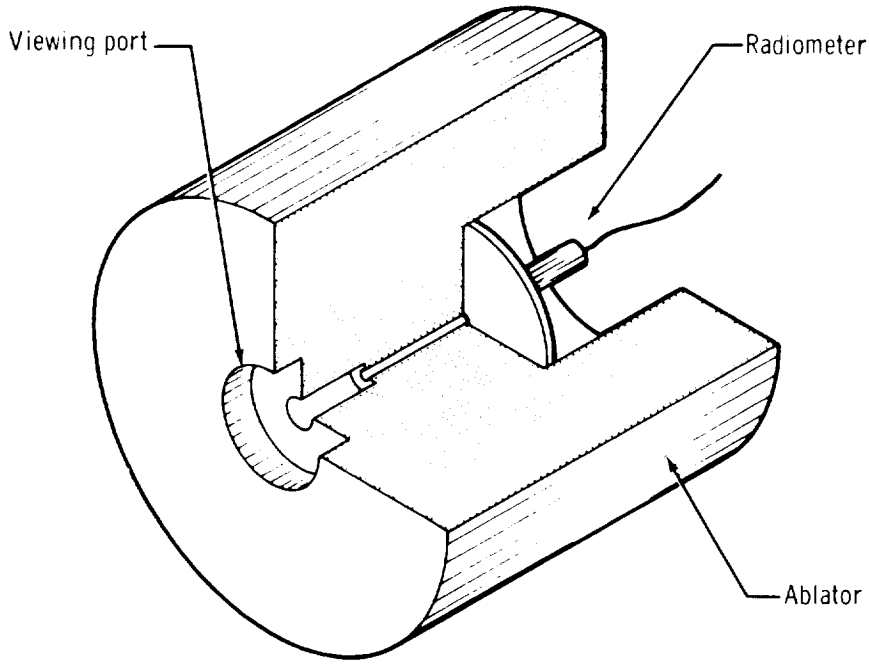

Figure B-5. - Sketch of radiometer model.

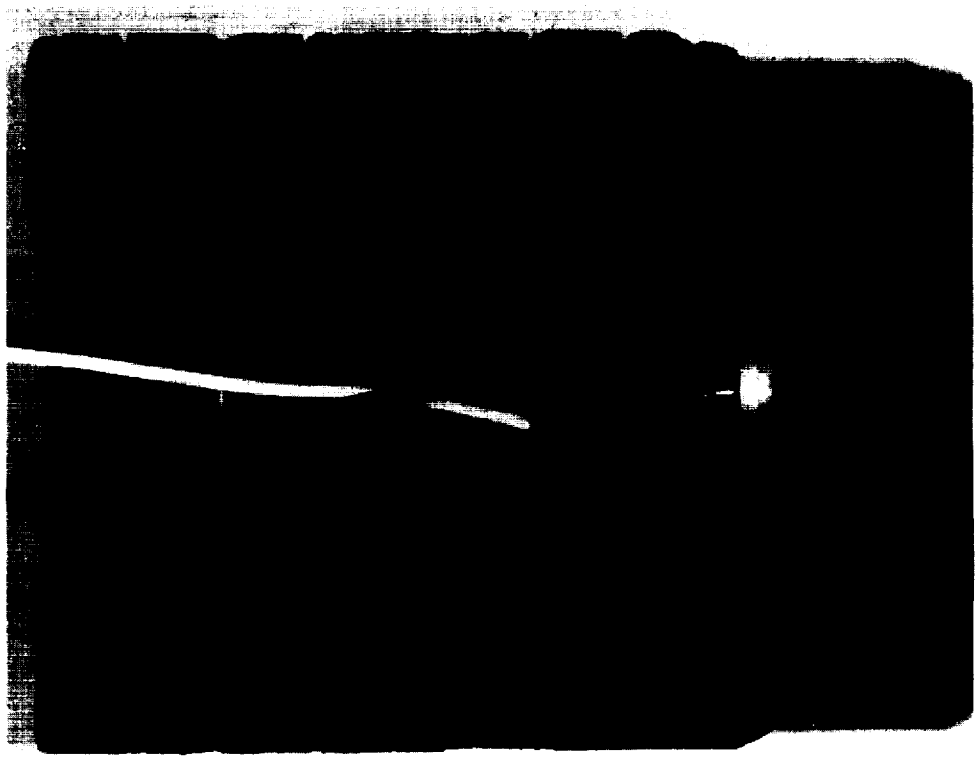

Figure B-6. - Post-test photograph of ablator-mounted radiometer.

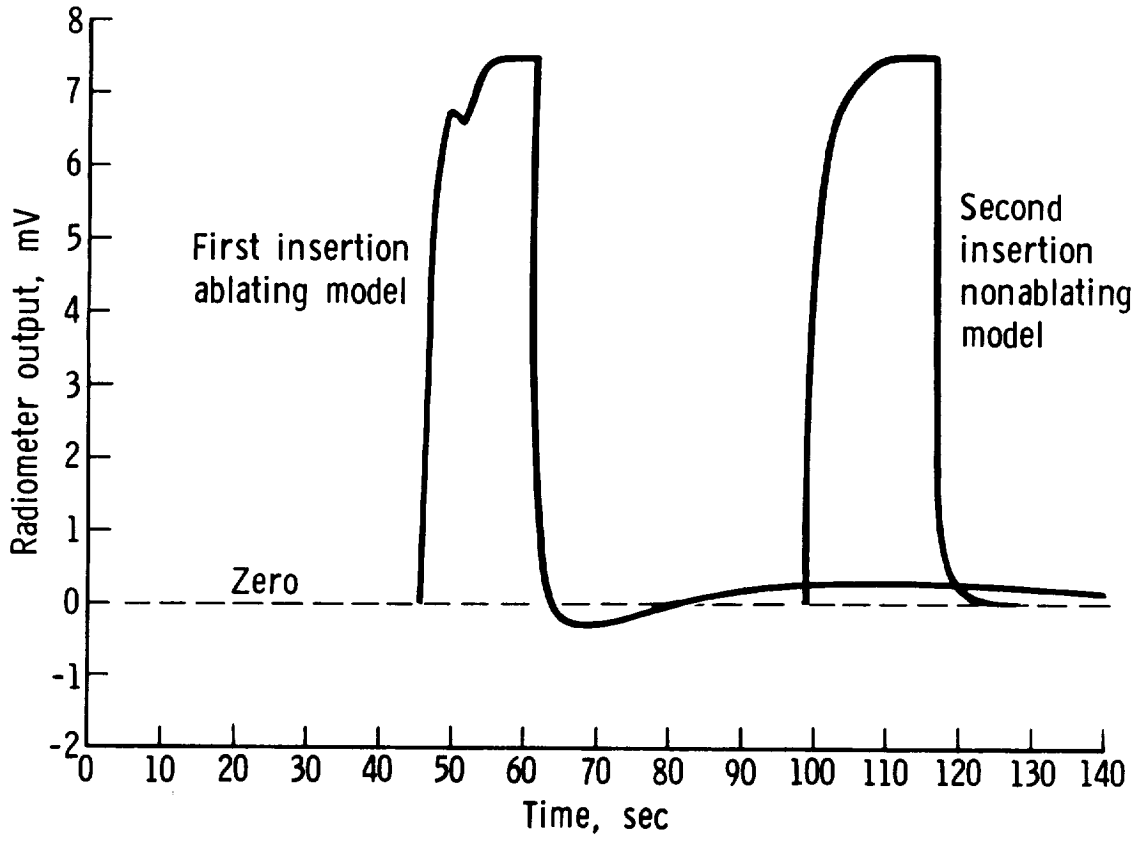

Figure B-7. - Comparison of ablating and nonablating models.

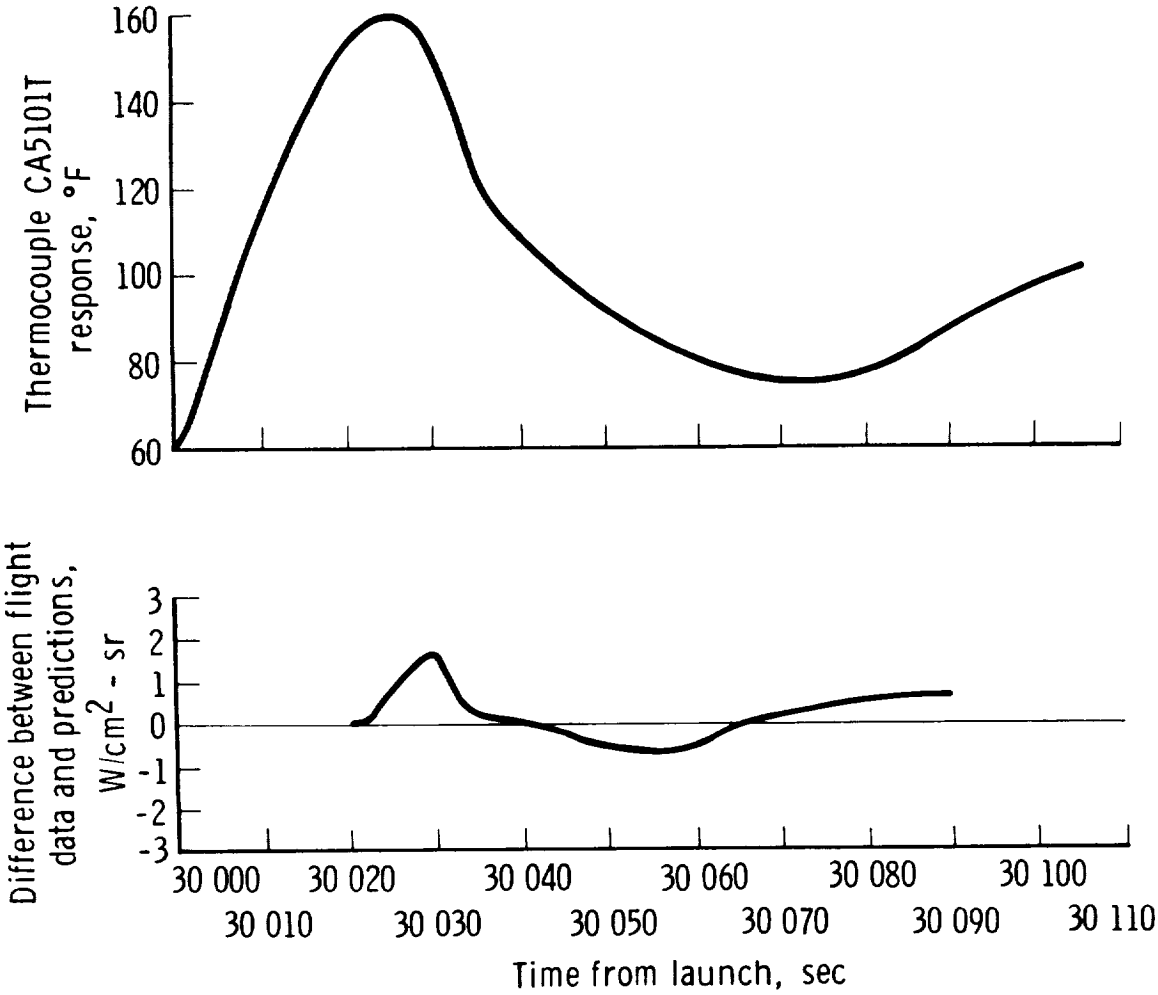

Figure B-8. - Influence of radiometer-body temperature.

NASA — MSC